

Recent Advances in Photocatalytic CO₂ Reduction into Valuable Products Using Nickel-Based Metal–Organic Frameworks

Elmehdi Moumen, Khaireddin Boukayouht, Redouane Haounati, Nor Aishah Saidina Amin, Wendy L. Queen, and Samir El Hankari*



Cite This: *J. Phys. Chem. Lett.* 2025, 16, 8173–8197



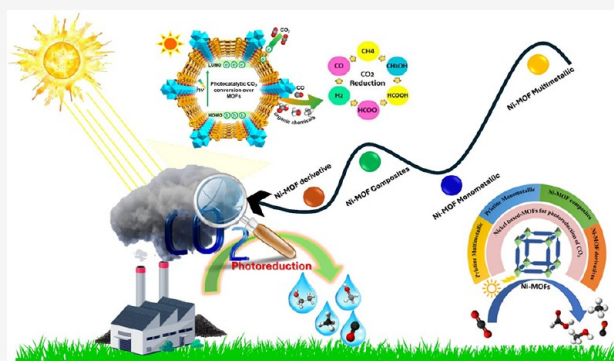
Read Online

ACCESS |

Metrics & More

Article Recommendations

ABSTRACT: The conversion of carbon dioxide into valuable chemicals through photochemical processes has been considered to be a potential technique to address environmental challenges. A good number of MOFs-based nickel (Ni-MOFs) compounds have garnered significant interest in the photocatalytic reduction of CO₂ due to their abundant active sites, tunable structure, the good affinity between CO₂, Ni elements, and other properties. This mini-review summarizes the different works on using Ni-MOFs as catalysts for the photocatalytic reduction of CO₂ by focusing on applying pristine, monometallic, and multimetallic Ni-MOFs. The advantages of combining Ni-MOFs with other potential semiconductors and their derivatives in improving the photocatalytic activity of the CO₂ reduction will also be discussed. Moreover, the challenges and opportunities associated with this class of materials for photocatalytic CO₂ reduction will be debated to inspire further research in this emerging field.



Excessive carbon dioxide emission caused by the huge consumption of fossil fuels leads to serious environmental problems, such as climate change, global warming, smoggy weather, and sea level rise, which are strongly related to the unrestricted development of human activities.¹ Thus, looking for novel and sustainable energy sources and the effective treatment of hazardous gases are important challenges that must be addressed.² Accordingly, various technologies and strategies have been developed to capture, store, and convert carbon dioxide via electrochemical, photochemical, and biological approaches.^{3–6} Therefore, the photocatalysis approach, by mimicking the photosynthesis process of green plants, inspired researchers to develop artificial photocatalysts for the photo-reduction of CO₂ to valuable chemicals.⁷ Up to now, extensive research has been focused on developing photocatalysts for the photoreduction of CO₂ to valuable chemicals. Titanium oxide (TiO₂) is considered the first explored photocatalyst by Fujishima and Honda⁸ and promoted the field of solar fuel production, which opened the door for many other successful attempts for various products over different photocatalysts including zeolite,⁹ metal oxide,¹⁰ cadmium sulfide (CdS)¹¹ as well as graphitic carbon nitride¹² and so on.^{13,14}

Recently, metal–organic frameworks (MOFs), commonly referred to as porous coordination polymers, have emerged as a class of crystalline porous hybrid materials constructed via the self-assembly of metal ions or metal clusters and organic ligands, triggering enormous research activities,^{15–20} especially photo-

conversion of CO₂ because of (i) the excellent CO₂ absorption capacity of MOFs, (ii) the presence of catalytically active metal sites in the structural diversity and tunability of MOF components, (iii) the high porosity of MOFs which provides diffusion of substrates to ensure their accessibility to the active sites, (iv) the high light-harvesting either by metal nodes or organic linkers in the framework and (v) the possibility of incorporating extra active sites within the framework by the functionalization of the parent structure of MOFs.^{21–24}

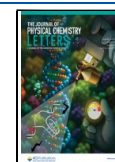
Among the most reported MOF-photocatalysts, transition metal-based MOFs appear to be efficient semiconductors in photocatalysis.^{25,26} In particular, Nickel-based MOFs (Ni-MOFs) have been designed and developed because of their low cost, good abundance of Nickel ions, and excellent photocatalytic properties.²⁷ Thus, many reviews have discussed the photocatalytic reduction and hydrogenation of CO₂ over pure MOFs, MOF composites, and MOF-derived nanomaterials, including transition metal-based MOFs and nontransition metal-based MOFs.^{28–38}

Received: March 26, 2025

Revised: July 15, 2025

Accepted: July 16, 2025

Published: August 4, 2025



However, to the best of our knowledge, no comprehensive reviews have specifically evaluated the performance of Ni-based MOFs, their composites, or their derivatives in photocatalytic CO₂ reduction. Owing to the redox flexibility, strong visible-light absorption, high CO₂ uptake capacity, and favorable electronic properties of Ni²⁺, which promote efficient electron mobility combined with the inherent structural tunability of MOFs, these materials offer distinct advantages over other MOF-based photocatalysts^{39,40}

Hence, in this mini-review, we aim to summarize the start of the art of Ni-MOFs, Ni-MOF composites, and their derivatives employed for the photocatalytic reduction of CO₂ and discuss their properties and their efficiency due to the considerable works published in the last seven years as illustrated in Figure 1. Finally, challenges and future perspectives on these materials for further research and application in photocatalytic CO₂ reduction will be addressed.

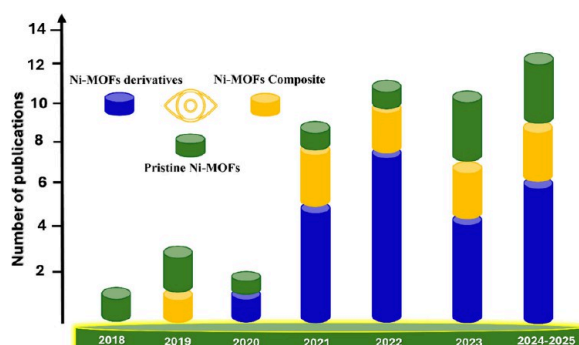


Figure 1. Number of papers of Ni-based MOFs for photocatalytic CO₂ reduction over time.

Mechanism of MOFs as Photocatalysts in CO₂ Reduction. Photocatalysis appears to be a revolutionary technology that facilitates redox reactions using UV or sunlight as an illuminating source to transform atmospheric CO₂ into chemical energy suitable for human use.⁴¹ The process of reducing CO₂ photocatalytically into valuable products takes place according to a refined mechanism in three stages. Initially, illumination prompts the generation of electron–hole pairs through light absorption. This is followed by the migration of these electrons (e[−]) and holes (h⁺) to the catalyst surface states. The final step witnesses these electrons engaging CO₂ at the surface, transforming it into various desired products.^{42,43} These products vary based on the CO₂ reduction reaction pathways (Table 1).⁴⁴ For the efficient change of CO₂ into targeted products using photocatalysis, the conduction band minimum (CBM) of the photocatalyst must exceed the energy level of the CBM of the final product at pH = 7.^{45,46} This requirement ensures that the electron transfer necessary for CO₂ reduction is energetically favorable, aligning with the conditions under which many photocatalytic reactions are designed to operate. Furthermore, photocatalysts that can absorb light within the visible spectrum, characterized by a bandgap of less than 3.2 eV, are considered to have a significant advantage for photocatalytic applications due to their efficiency in harnessing solar energy. A smaller bandgap below 3.2 eV allows for the absorption of a broader range of visible light wavelengths, thereby increasing the ability of photocatalysts to generate charge carriers (electrons and holes) that drive the CO₂ reduction process. As illustrated in Figure 2a, these principles highlight the interplay between the

Table 1. Depict the Transformation of CO₂ into Various Carbon-Derived Products in Aqueous Solution at a pH level of 7, with Reduction Potential References to the Normal Hydrogen Electrode (NHE) at 25 °C and 1 atm

Reaction	E° (V vs NHE at pH = 7)
CO ₂ (g) + e [−] → CO ₂ ^{•−} (aq)	−1.90
CO ₂ (g) + 2H ⁺ (aq) + 2e [−] → CO + H ₂ O(l)	−0.53
CO ₂ (g) + 2H ⁺ (aq) + 2e [−] → HCOOH(aq)	−0.61
CO ₂ (g) + 4H ⁺ (aq) + 4e [−] → HCHO(aq) + H ₂ O(l)	−0.48
CO ₂ (g) + 6H ⁺ (aq) + 6e [−] → CH ₃ OH(aq) + H ₂ O(l)	−0.38
CO ₂ + 8H ⁺ (aq) + 8e [−] → CH ₄ (g) + 2H ₂ O(l)	−0.24
2CO ₂ (g) + 10H ⁺ (aq) + 10e [−] → CH ₃ CHO(aq) + 3H ₂ O(l)	−0.36
2CO ₂ (g) + 12H ⁺ (aq) + 12e [−] → C ₂ H ₄ + 4H ₂ O(l)	−0.34
2CO ₂ (g) + 12H ⁺ (aq) + 12e [−] → C ₂ H ₅ OH + 3H ₂ O(l)	−0.33
2CO ₂ (g) + 14H ⁺ (aq) + 14e [−] → C ₂ H ₆ + 4H ₂ O(l)	−0.27
2H ⁺ (aq) + 2e [−] → H ₂ (l)	−0.41

CBM alignment, the bandgap of the photocatalyst, and the absorption of visible light. Lately, numerous research findings have shown that MOFs can be designed to serve as effective photocatalysts for the reduction of CO₂ and its transformation into valuable products.⁴⁷ The photocatalytic capabilities of MOFs stem from the interplay between their organic ligands and metal nodes, which likely act as sites for catalytic activity. These capabilities are propelled by the transfer of charge from ligands to metal and transitions of π – π^* electrons in the ligands due to light exposure.³⁷ With light irradiation, electrons move from the valence to the conduction band, generating holes, which is a hallmark trait of semiconductor behavior in MOFs, depicted in Figure 2b. In addition to semiconductors, other additives are crucial for the efficiency and sustainability of the photocatalytic process. Sacrificial agents such as triethanolamine (TEOA), for instance, contribute to maintaining the separation of charge carriers by donating electrons, thus assisting the photocatalyst's activity. The photosensitizer is also one of the important components of the photocatalytic system that plays a critical role in electron transfer after excitation by the absorption of photon energy in a broad range of wavelengths, from the UV (ultraviolet) to visible light region. Usually, metal-based photosensitizers are most prominent, such as tris(2,2′-bipyridyl) dichlororuthenium(II) hexahydrate (abbreviated as Rh-dye). Furthermore, in numerous MOFs, ligand-to-metal charge transfer (LMCT) and ligand π – π^* excitation occur within the ultraviolet (UV) and visible light regions. As a result, MOFs present promising opportunities for photocatalytic applications by incorporating diverse catalytic components, including photosensitizers and cocatalysts, into a unified solid material.^{48,49} The proposed mechanisms, such as ligand-to-metal charge transfer (LMCT) and synergistic effects in composite architectures, play a pivotal role in enhancing photocatalytic performance. Upon light irradiation, the organic linkers in MOFs can undergo π – π^* or n– π^* electronic transitions, which initiate LMCT by transferring excited electrons from the photoactive ligand to the metal centers. This electron delocalization facilitates efficient separation of charge carriers and prolongs the lifetime of excited states, which is critical for

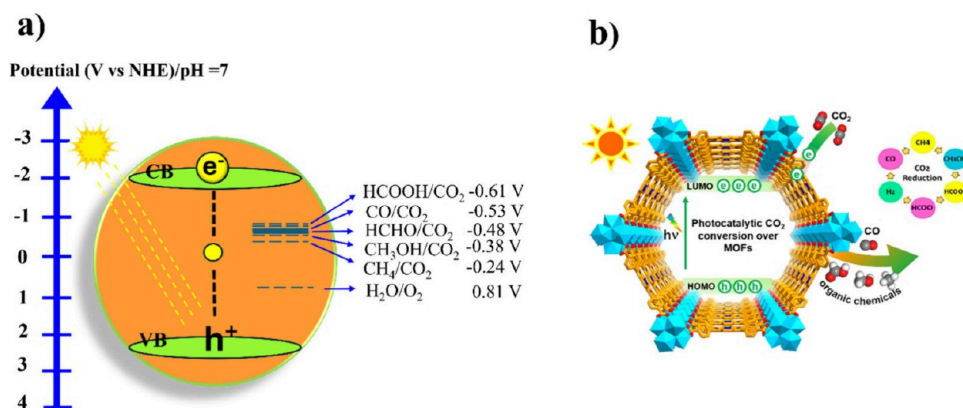


Figure 2. A schematic representation detailing the redox potential for transforming CO₂ into various outputs at a pH level of 7 for the metal–organic framework. b) Diagrammatic representations of the photocatalytic conversion of CO₂ to other substances via metal–organic frameworks. Adapted with permission from ref 48. Copyright 2020 Wiley.

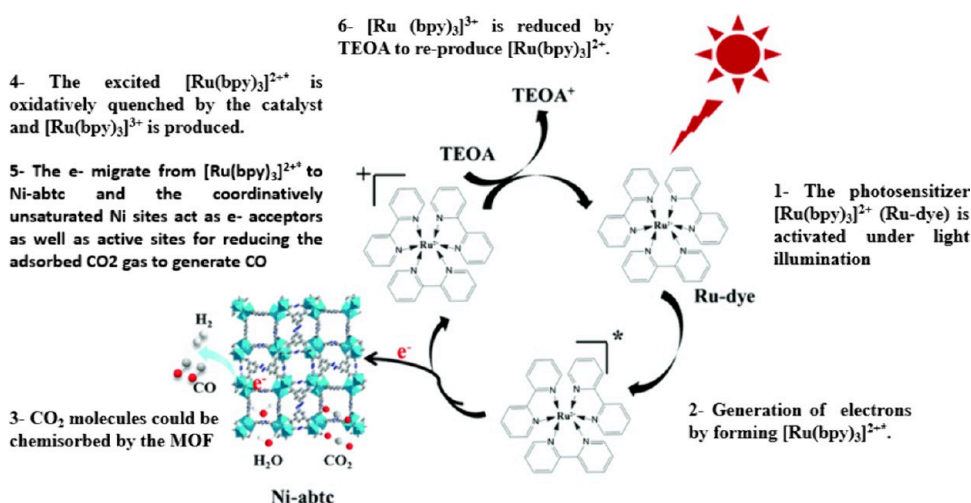


Figure 3. Diagram illustrating the different steps of photocatalytic conversion of CO₂ to CO by Ni-MOF-based photocatalyst in the presence of TEOA. Adapted with permission from ref 50. Copyright 2022 Royal Society of Chemistry.

downstream redox reactions. The LMCT process not only activates the metal nodes as electron reservoirs but also boosts the overall charge mobility within the MOF matrix. Additionally, when MOFs are engineered as composites with cocatalysts or photosensitizers, synergistic effects emerge that further improve the system's catalytic efficiency. These effects arise from optimized interfacial interactions, where the cocatalyst (e.g., metal nanoparticles or conductive supports) serves as an additional electron sink or transfer mediator, thereby minimizing charge recombination. Figure 3 illustrates the sequential steps in the photocatalytic reduction of CO₂ carried out by Ni-based MOF (Ni-abtc) under visible light irradiation, the photosensitizer tris(2,2'-bipyridyl)ruthenium(II) complex ([Ru(bpy)₃]²⁺) becomes photoexcited to an energetically active state ([Ru(bpy)₃]^{2+*}). This excited state undergoes oxidative quenching by transferring an electron to a nickel-based metal organic framework (Ni-abtc), generating [Ru(bpy)₃]³⁺. The Ni-abtc framework, which contains coordinatively unsaturated Ni²⁺ sites, serves both as an electron acceptor and as an active catalytic surface. These sites facilitate the adsorption (chemisorption) of CO₂ molecules, positioning them for efficient electron transfer and reduction to CO. Following electron transfer, the oxidized [Ru(bpy)₃]³⁺ species is regenerated to its original [Ru(bpy)₃]²⁺ state by the sacrificial electron donor

triethanolamine (TEOA). This regeneration step is essential for maintaining the photocatalytic cycle. The coordinated action of light-induced electron excitation, charge separation, and CO₂ chemisorption on the MOF framework enables efficient and selective reduction of CO₂ under mild conditions. The system demonstrates a promising approach for solar-driven carbon dioxide conversion using a molecular photosensitizer in conjunction with a MOF-based catalyst.^{50,51}

Pristine Ni-MOFs. Pristine MOFs have been extensively examined as potential candidates in the realm of photocatalytic CO₂ reduction in recent years.⁵³ Ni-MOFs, distinguished by their intricate microporous architecture, are engineered to promote the permeation of CO₂ molecules through the framework, directing them toward Nickel metal clusters strategically positioned to serve as the focal points for photocatalytic reactions aimed at CO₂ reduction. This unique structural configuration enables the efficient conversion of CO₂ by leveraging the nickel cluster's catalytic properties under light exposure.⁵⁴ Building on the foundation laid by monometallic Ni-MOFs, recent advancements in the field have introduced mixed metal MOFs, incorporating bimetallic and trimetallic systems while ensuring that Nickel remains the central catalyst within these frameworks.^{55,56} Such developments not only broaden the spectrum of photocatalytic activities but also improve their

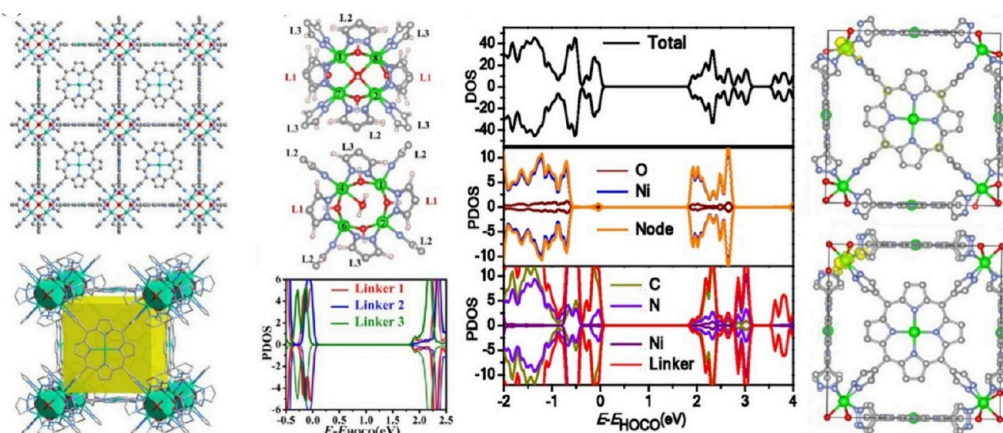


Figure 4. Crystal structure and corresponding void volume of the PCN-601. Exploration of charge transfer pathways and harvesting sites by performing theoretical calculations. Reproduced with permission from ref 65. Copyright 2020 American Chemical Society.

efficiency and selectivity in CO_2 reduction processes.⁵⁷ These mixed metal frameworks are tailored to enhance the structural diversity and functional capacity of MOFs, offering new avenues for optimizing photocatalytic performance through the deliberate manipulation of their compositional and structural attributes.^{58,59} Metals such as cobalt and iron can be integrated into the framework to function as additional catalytic sites, complementing the catalytic activity of nickel in the reduction of CO_2 . This synergistic effect between the metals can lead to a more efficient and possibly selective catalytic process, exploiting the unique properties of each metal involved.^{60,61} On the other hand, the introduction of metals such as titanium and zirconium is strategically aimed at bolstering the chemical stability of the MOFs.^{62,63} These elements contribute to the overall robustness of the structure, making it more resistant to degradation under the reaction conditions encountered during photocatalytic reactions. This enhancement in stability is crucial for the long-term application and effectiveness of MOFs in industrial settings.⁶⁴ Herein, we will discuss each category and highlight the benefits of creating additional defects within the bimetallic and trimetallic nickel-based MOFs, in addition to the effect of porosity and finally compare the nickel-based MOFs with other transition metal MOFs.

Monometallic Ni-MOFs. In a pioneering study, Fang et al. introduced the first pristine Ni-MOF utilizing a pyrazolyl porphyrinic ligand known as PCN-601 (Figure 4), representing a notable breakthrough in visible-light-induced photocatalytic CO_2 reduction. Notably, PCN-601 achieved an impressive CO_2 to methane conversion yield of $10.1 \mu\text{mol h}^{-1} \text{g}^{-1}$,⁶⁵ surpassing analogous MOFs using carboxylate porphyrin and the conventional Pt/CdS catalyst over 2 and 3 times, respectively. This is due to the integration of extra light harvesters ascribed to the porphyrin ligands and high porosity coupled with robust catalytic sites, which are attributed to the Nickel species either in the nodes of the framework or in the porphyrin center.⁴⁸ The PCN-601 demonstrated a constant methane yield through a span of 5 reaction cycles (10 h for each cycle), and high-rate production of CH_4 then CO , suggesting good stability and selectivity of this photocatalyst toward CH_4 .⁶⁵ Further insights into the charge transfer behavior within PCN-601 were provided by electron paramagnetic resonance (EPR) spectroscopy and density functional theory (DFT) calculations. EPR spectra under visible-light irradiation revealed enhanced Ni(I) signals, indicating the photoinduced reduction of Ni centers. Since Ni atoms are present in both the porphyrin ligand and the metal

node in PCN-601, theoretical calculations were carried out to gain deeper insight into its structural characteristics. Within the unit cell of PCN-601, the metal node $[\text{Ni}_8(\text{OH})_4(\text{H}_2\text{O})_2]$ (abbreviated as $[\text{Ni}_8]$) is coordinated by 12 porphyrin ligands through pyrazole linkages. These ligands extend in three spatial directions, designated as L1, L2, and L3 (as illustrated in Figure 4). Theoretical analyses showed that the highest occupied molecular orbitals (HOMO) are primarily localized on the porphyrin ligands, while the lowest unoccupied molecular orbitals (LUMO) are shared between the Ni_8 metal-oxo nodes and the ligands. This electronic structure facilitates two excitation pathways: ligand-localized excitation and ligand-to-node charge transfer. Photogenerated electrons readily migrate from the porphyrin ligands to the Ni_8 nodes, with holes remaining on the ligands, enabling efficient charge separation. Modeling of the excited states further localized the photoexcited electrons on individual Ni atoms within the metal nodes, confirming these nodes as the main electron-harvesting sites of PCN-601 (Figure 4). This ligand–node electronic interplay is key to the high photocatalytic activity and stability observed in PCN-601.

Later, another work emphasized the role of nickel over other transition metal-based by comparing the CO_2 photoreduction of Ni-MOF with its counterpart cobalt MOF (Co-MOF) using the same ligand of 3,3',5,5'-azobenzene tetracarboxylic acid (H_4abtc).⁵⁰ The Ni-MOF (Ni-abtc) catalyst obtained by mixing H_4abtc and the nickel chloride demonstrated good performance for the rate of CO_2 photoreduction yielding $19.13 \mu\text{mol h}^{-1}$ of CO , with a selectivity of 91.4%. In contrast, the Co-abtc photocatalyst exhibited a moderate performance toward CO_2 photoreduction to CO of $11.6 \mu\text{mol h}^{-1}$ and a minimal CO selectivity of 40.1% under the same photocatalytic conditions.

Later an alternative approach involving the photocatalytic reduction of CO_2 toward CO was explored by using three novel Ni(II)-bipyridine complexes: Ni-1 ($[\text{NiCl}_2(4,4'\text{-dichloro-2,2'}\text{-bipyridine})_2]$), Ni-2 ($[\text{NiCl}_2(4,4'\text{-dibromo-2,2'}\text{-bipyridine})_2]$), and Ni-3 ($[\text{NiCl}_2(4,4'\text{-diphenyl-2,2'}\text{-bipyridine})_2]$).⁶⁶ Their investigation employed a mixture of acetonitrile and water as the reaction medium, using tris(bipyridine) ruthenium(II) chloride as the photosensitizer and 1-benzyl-1,4-dihydronicotinamide as the electron provider. The Ni-1 demonstrated significantly enhanced catalytic activity under visible light irradiation, in contrast to the conventional homogeneous Ni-bipyridine catalysts. Additionally, the mechanism for Ni-1's photocatalytic CO_2 transformation to CO is depicted in Figure

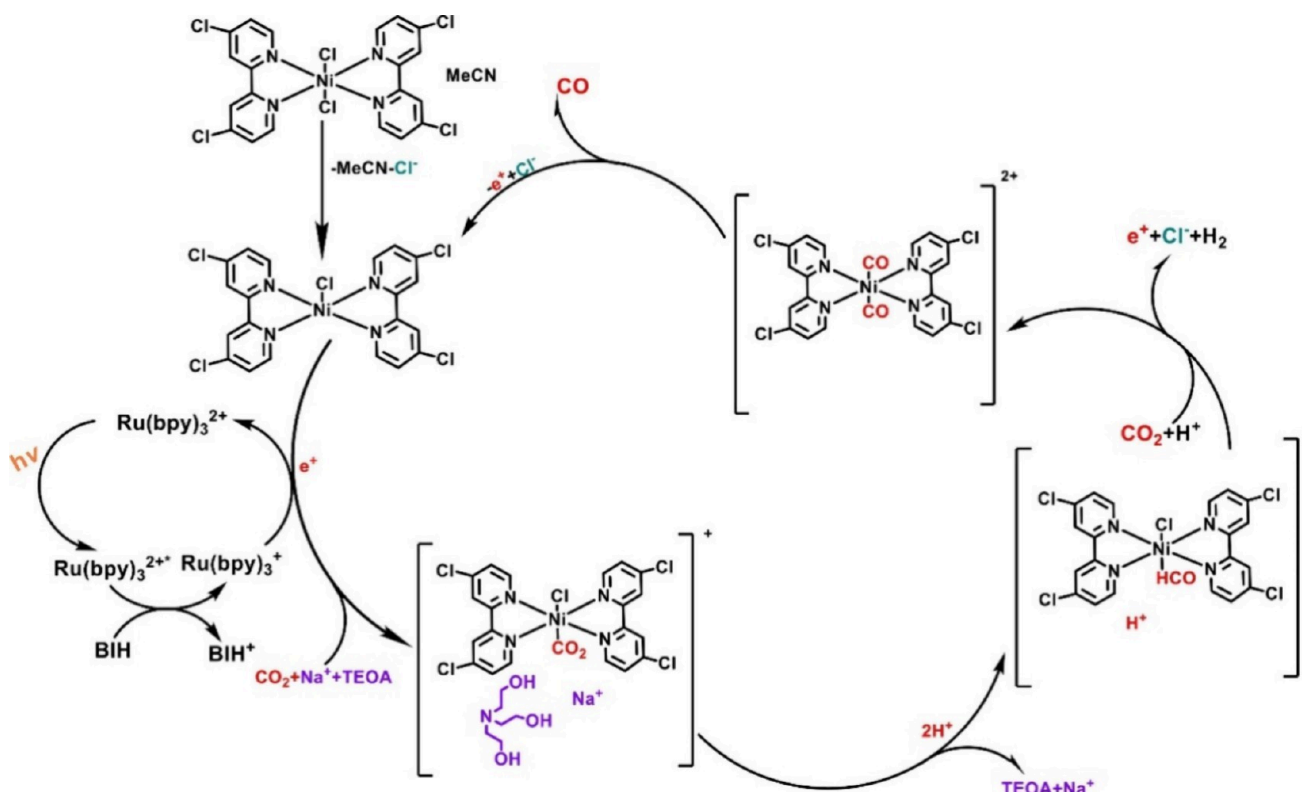


Figure 5. Proposed mechanism for Ni-1 mediated photocatalytic CO₂ reduction. Reproduced with permission from ref 66. Copyright 2023 The Authors.

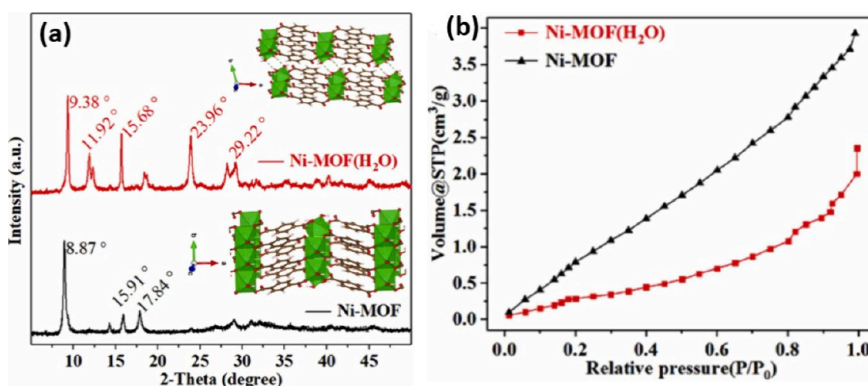


Figure 6. (a) XRD patterns of Ni-MOF(H₂O) and Ni-MOF with corresponding diagram representations of their crystal structures and (b) CO₂ adsorption curves. Reproduced with permission from ref 40. Copyright 2022 Elsevier.

5. When exposed to visible light, [Ru]²⁺ is excited to its [Ru]^{2+*} state, which is subsequently reduced to [Ru]⁺ via BIH. This reduced [Ru]⁺, after coupling with protons, is renewed to [Ru]²⁺. In the next step, CO₂ interacts with the reduced nickel center via the carbon atom, forming a Ni-CO₂ complex. Then, the protonation of this complex produces a formyl group (HCO), which subsequently undergoes a proton loss to generate CO, completing the catalytic cycle. To further elucidate the enhanced activity of Ni-1, DFT calculations were conducted. These revealed that Ni-1 has the highest CO₂ binding energy among the three complexes, making the Ni-CO₂ bond more stable and increasing the likelihood of successful CO₂ activation and conversion. Additionally, Ni-1 exhibited the most favorable HOMO–LUMO energy alignment with CO₂, facilitating efficient charge transfer during photocatalysis. The reduced catalytic activity observed for Ni-3 was attributed to its lower

CO₂ binding energy and significant structural deformation upon adsorption. These computational insights highlight the critical role of ligand substituents in modulating the electronic properties of the Ni center and provide a theoretical basis for the superior photocatalytic performance of Ni-1.

After these works on Ni-MOF for photocatalytic reduction, other studies highlighted why it is important to have the 2D structure,⁶⁷ the effect of crystals form of the MOFs,^{40,68} and how to broaden the adsorption of light.³⁹ The 2D nanosheets have also been considered as a successful route to enhance the photocatalytic productivity of CO₂ reduction by favoring the rapid mass transport and superior electron transfer due to their (i) low thickness, which facilitates the light transmittance through the MOFs; (ii) enhanced conductivity to assist the electron migration to the metal centers; and (iii) extensive exposure of active centers promoting surface redox reactions.

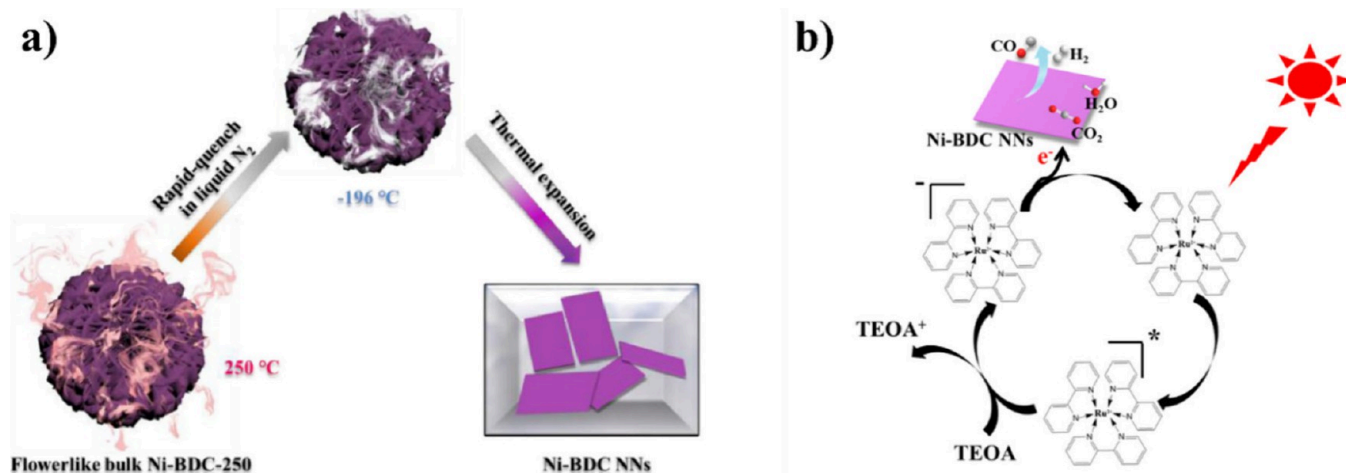


Figure 7. Fabrication of Ni-BDC nanosheets carried out using a thermal expansion method (a). Proposed mechanism for CO₂ reduction using Ni-BDC NNs under visible light illumination (b). Reproduced with permission from ref 69. Copyright 2022 Published by Elsevier on behalf of Chinese Chemical Society and Institute of Materia Medica, Chinese Academy of Medical Sciences.

For instance, the construction of Ni-BDC 2D nanosheets with the assistance of supercritical CO₂ showed a high CO yield of 104000 $\mu\text{mol g}^{-1} \text{h}^{-1}$, which is two times superior to the bulky Ni-BDC with a selectivity of 96.8%.⁶⁷

The importance of having Ni-MOF with layered and 2D structures is also demonstrated by synthesizing the bulky Ni-MOF and two Nickel metal–organic layers Ni-MOL-100 and Ni-MOL-010 with different uncovered crystal facets 100 and 010, respectively.⁶⁸ The Ni-MOL-100 showed the best photocatalytic activity of CO₂ to CO up to 11890 $\mu\text{mol g}^{-1}$ for 4 h with 96.2% selectivity compared to two other Ni-MOFs (Ni-MOL-010 and bulky Ni-MOF). It also showed good stability over 4 runs of the photocatalytic CO₂ reduction reaction. In another study, two Ni-MOFs exhibiting distinct crystal structures were fabricated and subsequently examined in the reduction of CO₂ via photocatalysis.⁴⁰ While the Ni-MOF(H₂O) with replicated crystal unit chains [Ni(1)O₆]₂Ni(2)O₆, where the Ni atoms are connected to six oxygen atoms to form octahedrons or bonded by 4 O atoms from a linker and 2-OH, the Ni-MOF with repeated unit of [Ni₂(OH)₂(C₈H₄O₄)] belongs to the monoclinic system and presents two varieties of Ni atoms exhibiting diverse integration surroundings. But both Ni atoms coordinate in groups of six, forming interconnected octahedrons in the (100) crystal plane, resulting in 2D Ni layers (Figure 6a). This slight difference in the structures provides the Ni-MOF(H₂O) with better CO₂ adsorption performance than that of Ni-MOF (Figure 6b); thus, Ni-MOF(H₂O) registered a maximum CO production rate of 9610 $\mu\text{mol h}^{-1} \text{g}^{-1}$ and a selectivity of 95.24% toward CO compared to the Ni-MOF (8100 $\mu\text{mol h}^{-1} \text{g}^{-1}$). Ni-MOF(H₂O) could maintain its photocatalytic activity for at least 5 h, suggesting excellent structural stability.⁴⁰

Other MOF nanosheets with 2D structures were developed by using a thermal expansion method (Figure 7a).⁶⁹ Their study presents an effective top-down approach for synthesizing Ni-BDC nanosheets through a novel method of thermal expansion followed by rapid quenching in liquid nitrogen applied to flowerlike bulky MOFs. For instance, the thermally expanded Ni-MOF nanosheets displayed efficient CO generation (7000 $\mu\text{mol h}^{-1} \text{g}^{-1}$) under visible light with negligible H₂ evolution. This selectivity can be attributed to several factors: (i) the preferential binding affinity of Ni(II) sites toward CO₂ over

protons with more negative adsorption energies for CO₂; (ii) the spatial confinement and electronic environment within MOF structures, which can sterically hinder proton access to catalytic centers; and (iii) the engineered band alignment that facilitates electron transfer to CO₂ rather than to protons. Additionally, the delocalization of photogenerated electrons through conjugated linkers and their directional migration toward Ni centers enhances the CO₂ activation while suppressing the hydrogen evolution reaction (HER). These findings suggest that the rational design of the coordination environment and electronic structure in Ni-based MOFs plays a pivotal role in promoting CO₂ reduction over competing HER pathways.^{69,70} A proposed method for reducing CO₂ through photocatalysis over Ni-BDC nanosheets is illustrated (Figure 7b). The photosensitizer [Ru(bpy)₃]²⁺ is excited to produce the [Ru(bpy)₃]^{2+*} state, which is rapidly reduced by the sacrificial electron donor TEOA. The reaction is initiated with the reduction of [Ru(bpy)₃]³⁺ to [Ru(bpy)₃]⁺. This species then transfers electrons to the few-layered Ni-BDC nanosheets, which possess numerous Ni sites with incomplete coordination crucial for CO₂ adsorption, which plays a pivotal role in the photocatalytic process. In other words, Ni-BDC nanosheets exhibit strong CO₂ adsorption, resulting in the creation of CO₂ adducts such as Ni-CO₂. Previous research highlights that the utilization of these CO₂ adducts, culminating in the production of CO, represents the rate-limiting step in the catalytic reaction.^{71,72} Consequently, Ni-BDC nanosheets demonstrate significant activity in the deoxygenated reduction of CO₂.

Lately, two MOFs with 2D using succinic acid (SA) as a low-cost ligand and nickel or cobalt as a metal were developed to synthesize inexpensive photocatalyst-based MOFs.⁷³ The resulting Ni-SA and its isostructural analog Co-SA served as photocatalysts for CO₂ reduction under LED illumination ($\lambda > 410 \text{ nm}$) and exhibited a CO manufacture rate of 6960 and 1050 $\mu\text{mol g}^{-1} \text{h}^{-1}$, respectively, accompanied by an insignificant amount of H₂.⁷³

Furthermore, the integration of light-harvesting functionality was shown to be effective not only for enhancing CO₂ adsorption but also for broadening the absorption spectrum of light. Indeed, this was emphasized by incorporating amino (–NH₂) groups into the organic linkers of MOFs, particularly by using 2'-amino-5'-(4-carboxyphenyl)-[1,1':3',1''-terphenyl]-

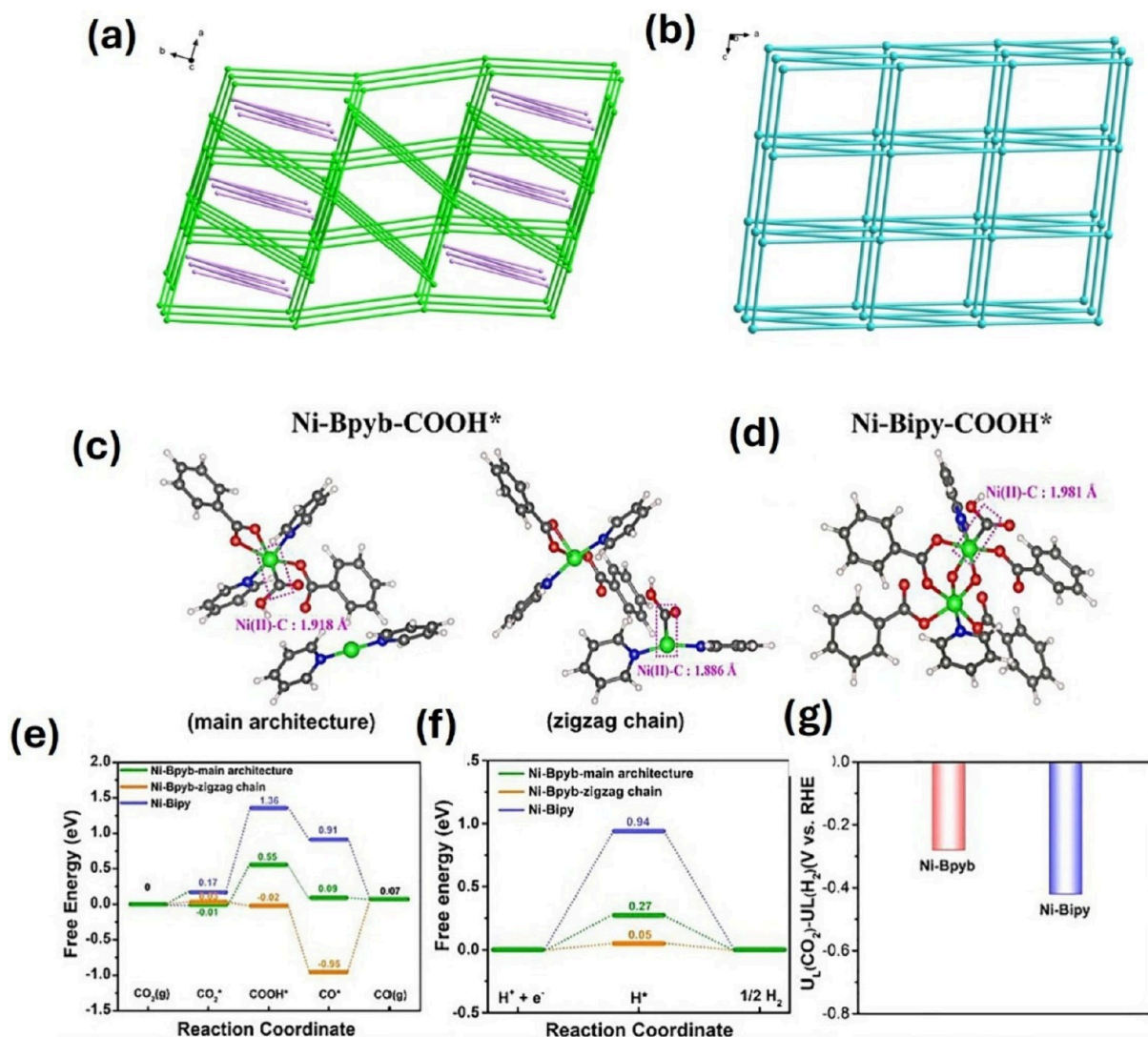


Figure 8. (a,b) Ni-Bpyb: Ni1 (green) and Ni2 (purple) sites. Ni-Bipy: dimer units $[\text{Ni}_2(\text{COO})(\mu_2\text{-H}_2\text{O})_2]$ shown as aqua spheres. (c,d) The bond lengths of Ni(II)-based MOFs-COOH*. (e,f) Calculated CO₂RR and HER free energy diagrams. (g) The difference in limiting potentials (UL(CO₂)-UL(H₂)) for the selectivity of CO₂ reduction relative to H₂ on Ni-based MOFs). Reproduced with permission from ref 45. Copyright 2022 Published by Elsevier.

4,4'-dicarboxylic acid (NH₂-BTBH₃) for the synthesis of amino-functionalized Ni-MOFs, with 1,4-bis(4-pyridyl)benzene (Bpyb) or 4,4'-bipyridine (Bipy), designated as Ni-Bpyb and Ni-Bipy, respectively. The structure shows that each NH₂-BTB³⁻ links two Ni(II) ions, with one -COO⁻ group uncoordinated. Bpyb bridges Ni(II) centers to form a 3D anionic framework with elliptical and hexagonal channels. The Ni-Bpyb network adopts a 4-connected uninodal {6⁵.8} topology (Figure 8a,b). Comparative analysis revealed that both materials functioned as productive photocatalysts for the transformation of CO₂ into CO.³⁹ While the Ni-Bpyb exhibited an excellent CO yield of 1326.7 $\mu\text{mol g}^{-1} \text{h}^{-1}$ under visible-light illumination with elevated selectivity (98.80%) and the photocatalytic activity stayed consistent over three consecutive cycles, the Ni-Bipy showed a CO formation rate of 653.6 $\mu\text{mol g}^{-1} \text{h}^{-1}$ with selectivity of 97.89%. The apparent quantum efficiency (AQE) measurement is reported as 2.12%@420 nm which is the supreme obtained record amidst the MOF-based photocatalysts for CO₂ reduction indicating how the amine group enhances the light-harvesting.³⁹

In addition, the superior CO₂ reduction activity of Ni-Bpyb compared to Ni-Bipy, was explained via DFT calculations by analyzing the thermodynamic parameters governing the CO₂ reduction reaction (CO₂RR) (Figure 8c-g). However, Ni-Bpyb exhibited more favorable CO₂ adsorption energies (-0.01 and +0.03 eV) than Ni-Bipy (0.17 eV), indicating stronger CO₂ binding at the Ni(II) active sites. Furthermore, the free energy barrier for the rate-determining step of CO₂* to COOH* was significantly lower for Ni-Bpyb (+0.56 eV and -0.05 eV for main and zigzag architectures, respectively) than for Ni-Bipy (1.19 eV), suggesting enhanced catalytic efficiency. Additionally, shorter Ni-C bond lengths in the Ni-Bpyb-COOH* intermediate (1.918 and 1.886 Å) compared to Ni-Bipy (1.981 Å) further confirmed stronger interaction with key intermediates. These factors collectively explain the enhanced CO production activity and selectivity of Ni-Bpyb under visible-light irradiation. In contrast, the binding and activation of H₂O for hydrogen evolution are less thermodynamically favorable at the Ni(II) sites of Ni-Bpyb. These factors shift the reaction selectivity toward CO₂-to-CO conversion, minimizing the

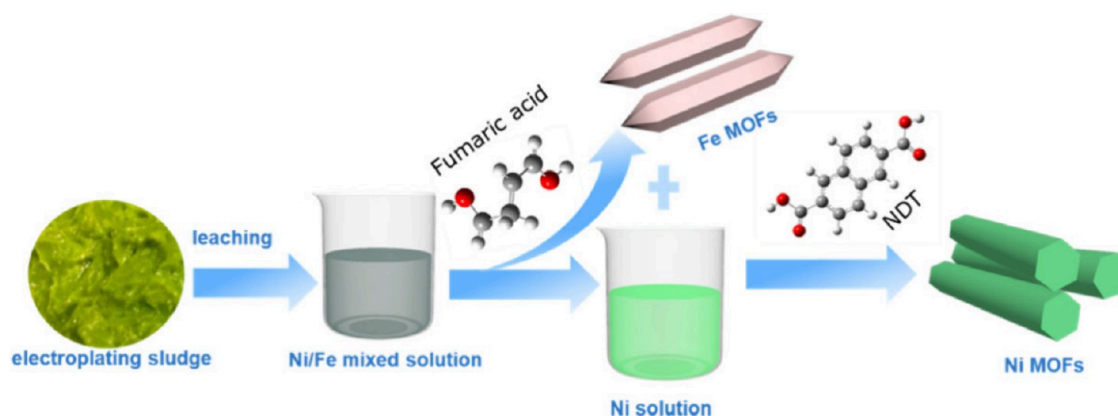


Figure 9. Gradient recovery method for sequential fabrication of Fe-MOFs and Ni-MOFs synthesized from electroplating sludge employing fumaric acid (FA) and 2,6-naphthalenedicarboxylate tetrahydrate (NDT) as organic ligands. Reproduced with permission from ref 75. Copyright 2020 Elsevier.

competing H_2 generation and thereby enhancing overall photocatalytic selectivity in Ni-based MOFs.⁴⁵

Although the development of MOFs is encouraging, the high cost of some organic ligands and some metal precursors used for the construction of MOFs motivated researchers to look for other ways to convert waste to valuable precursors needed for the preparation of MOFs.²⁰ In this regard, repurposing electroplating sludge and waste PET resulted in the preparation of Ni-MOF-W nanocrystals, which demonstrated an outstanding performance facing the photoreduction of CO_2 , providing $9680 \mu\text{mol h}^{-1} \text{g}^{-1}$ of CO with 96.7% selectivity over H_2 evolution, and recycled 5 times.⁷⁴ This work opened the door for other researchers to convert industrial waste into different MOFs, especially Ni-MOF, which was delicately prepared from Fe/Ni-contained electroplating sludges beside the Fe-MOF using the gradient recovery approach (Figure 9).⁷⁵ In this work the capability of those MOFs in the conversion of anthropogenic CO_2 under LED light illumination ($400 \text{ nm} \leq \lambda \leq 800 \text{ nm}$) was evaluated, and they discovered that the newly synthesized Ni-MOF displays the best enhancement in CO_2 photoconversion (CO production rate = $13.6 \mu\text{mol h}^{-1}$) among Fe-MOF and FeNi-MOF with different ratio of Ni/Fe, whereas Fe-MOF exhibits a preference for hydrogen production, of $11.4 \mu\text{mol h}^{-1}$.⁷⁵

The use of Ni element in the formation of MOF photocatalysts provides catalysts with high photocatalytic effectiveness. However, the wise selection of linkers, the crystal forms of Ni-MOF results, and its relationship with the synthesized process as well as the cost should be investigated to improve the CO_2 photoreduction activities. While monometallic Ni-MOFs have demonstrated promising photocatalytic performance in CO_2 reduction, they still face inherent limitations, such as suboptimal charge separation, limited light absorption range, and potential stability issues under prolonged irradiation. These challenges highlight the need for rational design strategies that go beyond single-metal systems. Incorporating additional metal centers into the MOF framework can introduce synergistic effects, enhance charge transfer dynamics, and improve catalytic robustness. Therefore, to address these limitations and further boost photocatalytic efficiency, recent research has shifted toward the development of polymetallic Ni-based MOFs, as discussed in the following section. A better overall comparison of various Ni-MOFs is shown in Table 2.

Multimetallic Ni-MOFs. Recently, many researchers have demonstrated that bimetallic or trimetallic MOFs can significantly enhance the photocatalytic CO_2 reduction activity by tuning the molar ratio of the mixed metals in the targeted MOF.^{76–81} This effect can be turned by applying the polarization effect,⁷⁹ or controlling the morphology of the materials.⁸⁰

Taking this into consideration, Ni metal ions were integrated into titanium oxo clusters of $\text{NH}_2\text{-MIL-125(Ti)}$ with diverse Ni/Ti compositions (Figure 10).⁷⁶ X-ray diffraction (XRD) analysis (Figure 10a) confirmed the successful integration of Ni into the Ti-MOF structure, with phase transitions evident at increasing Ni content. Scanning electron microscopy (SEM) images (Figure 10b) revealed morphological evolution from uniform Ti-MOF particles to more complex architectures in Ni-MOF and mixed-metal NT samples, with the 75% Ni–Ti sample displaying a well-structured morphology favorable for photocatalysis. The resulting Ni/Ti bimetallic MOFs with 75% Ni metal ions (75%NiTi-MOF) displayed the best photocatalytic CO_2 reduction performance among other ratios of Ni–Ti-MOF with CO and CH_4 productivity of 13.37 and $0.35 \mu\text{mol h}^{-1} \text{g}^{-1}$, respectively (Figure 10c). The proposed charge transfer mechanism (Figure 10d) involves light-induced ligand-to-metal charge transfer (LMCT) processes at both Ti and Ni centers, followed by efficient intermetallic charge transfer that enhances electron separation and mobility. A schematic representation (Figure 10e) illustrates that these photogenerated electrons facilitate the selective reduction of CO_2 to CO, CH_4 , and H_2 . This cooperative effect between bimetallic centers underscores the potential of rationally designed MOFs for efficient solar-driven CO_2 conversion.

This demonstrates the superior product selectivity of Ni/Ti bimetallic MOFs exceeding 85% for CO_2 to CO. Besides titanium metal, iron metal has shown high catalytic efficiency and high visible-light response when combined with Ni-MOF using 2,5-dihydroxy terephthalic acid ligand.⁸² Among a sequence of Fe/Ni-MOFs featuring a core–shell structure hydrothermally synthesized by adjusting the synthesis temperature and time, Fe/Ni-T120 exhibited an effective photocatalytic process for reducing CO_2 even after repeated cycles. It displayed a CO evolution rate of $9740 \mu\text{mol g}^{-1} \text{h}^{-1}$, and the selectivity reached up to 92.1% when employing TEOA as sacrificial catalysts and $[\text{Ru}(\text{bpy})_3]\text{Cl}_2 \cdot 6\text{H}_2\text{O}$ used as photosensitizing agent.⁸²

Table 2. Performance Analysis of Pristine Ni-MOFs, and Ni-MOF Composites for Photocatalytic Reduction of CO₂^a

Photocatalyst	Synthesis of MOF	Feed composition	Light source	Product	Ref
PCN-601	Solvothermal: Ni(CH ₃ COO) ₂ ·4H ₂ O (0.4 g), H ₄ TTP (0.2 g), Et ₃ N (1 mL), and H ₂ O (4 mL) in 40 mL DMF; ultrasonicated, then heated at 75 °C for 4 days. Product centrifuged, washed with DMF, soaked in acetone (24 h), and vacuum-dried at 40 °C	5 mg Catalyst, 3 mL water (vapor), 80 kPa CO ₂ , 10 h, RT (20 °C)	xenon lamp, UV-cut filter (λ ≥ 410 nm)	CH ₄ = 10.1 μmol h ⁻¹ g ⁻¹	65
Ni-MOL-100	Solvothermal: H ₂ BDC (1.0 mmol) in DMF (5 mL); Ni(NO ₃) ₂ ·6H ₂ O (1.5 mmol) in 10 mL DMF added dropwise, followed by NaOH (0.08 mmol in 2 mL H ₂ O). Stirred 1 h, heated at 120 °C for 10 h. Product filtered, washed with DMF and alcohol, and dried at 50 °C	1 mg catalyst, [Ru], 0.2 mL TEOA, 4 mL MeCN, 1 mL H ₂ O at RT	xenon lamp (300 mW, λ > 420 nm)	CO = 11890 ± 0.65 μmol g ⁻¹ for 4 h	68
Ni-MOF-W	Solvothermal: BDC (1.5 mmol) and NiCl ₂ ·6H ₂ O or Ni(aq) (1.5 mmol) in DMF/EtOH/H ₂ O (64:4:X mL); stirred and heated at 140 °C for 24 h. Product collected by centrifugation, washed with H ₂ O/EtOH, and freeze-dried	1 mg catalyst, 7.5 mg of [Ru], 1 mL TEOA, 2 mL H ₂ O, 3 mL MeCN	SW white LED (400–1000 nm)	CO = 9680 μmol h ⁻¹ g ⁻¹	74
Ni-MOF(H ₂ O)	Solvothermal: Ni(OH) ₂ (0.51 mmol) and BDC (0.51 mmol) in DMF/H ₂ O (1:1, 40 mL); ultrasonicated 5 min, refluxed at 90 °C for 6 h (500 rpm). Product centrifuged, washed with H ₂ O and DMF, and vacuum-dried at 50 °C overnight	1.0 mg catalyst, 7.5 mg photo-sensitizer [Ru], 3 mL MeCN, 2 mL H ₂ O, 1 mL TEOA	5 W white LED lamp 400–1000 nm	CO = 9610 μmol h ⁻¹ g ⁻¹ CO = 8100 μmol h ⁻¹ g ⁻¹	40
Ni-MOF	Hydrothermal: Ni(DPA) ₂ (21 μL, 1 M), FF (40 μL), and NaOH (15 μL, 1 M) in H ₂ O (5 mL); stirred, then heated at 80 °C for 24 h. Product washed with ethanol and dried	RT, 10 mg of the samples, the pressure inside the reactor reached 75 kPa, 0.4 mL of deionized water	300 W xenon lamp	CO = 11.75 μmol h ⁻¹ g ⁻¹	79
Ni(DPA) ₂	Ultrasound-Hydrothermal: Small-size Ni-MOF: same as above, with 3 h sonication (40 kHz) before heating			CO = 7.2 μmol h ⁻¹ g ⁻¹	
Co _{0.1} Ni _{0.9} -MOF	Co-doped MOF: Co _{0.1} Ni _{0.9} -MOF: same as small-size Ni-MOF, with Co(NO ₃) ₂ (0.1 M) added to achieve Co/Ni atomic ratios of 5–30%			CO = 38.74 μmol h ⁻¹ g ⁻¹	
Ni-abtc	Solvothermal: NiCl ₂ ·6H ₂ O (237 mg) and H ₄ btc (184 mg) in DMF/EtOH/H ₂ O (32:2:2 mL); heated at 140 °C for 2 days. Product filtered, washed with DMF and H ₂ O. Yield: 80.3% (based on NiCl ₂ ·6H ₂ O)	1 mg of photocatalyst, 7.5 mg of [Ru], 1 mL of TEOA, 3 mL MeCN, 2 mL of H ₂ O, 1 atm, 30 °C	300 W xenon-lamp cutoff filter (λ ≥ 410 nm)	CO = 19130 μmol h ⁻¹ g ⁻¹	50
Nickel(II)-bipyridine	Solvothermal: Ni(PPH ₃) ₂ Cl ₂ (0.05 mmol) and 4,4'-dichloro-2,2'-bipyridine (0.1 mmol) in acetonitrile (4 mL); heated at 140 °C for 30 min. Product (Ni-1) isolated as green crystals (94% yield)	6 mL of a 4:1:1 (v/v/v) mixture of MeCN, water and TEOA	460 nm LED blue light	CO = 34602.4 μmol h ⁻¹ g ⁻¹	66
Ni-BDC 2D nanosheets	Solvothermal: H ₂ BDC (0.7 mmol), Ni(NO ₃) ₂ ·6H ₂ O (0.7 mmol), DMF (10 mL), H ₂ O (0.6 mL), 140 °C for 12 h	1.0 mg catalysts, 0.05 mM [Ru], 12 mL water, 18 mL MeCN, 6 mL TEOA, 25 °C	300 W xenon lamp (λ > 420 nm)	CO = 104000 μmol h ⁻¹ g ⁻¹	67
Ni-Bpyb	Solvothermal: Ni(NO ₃) ₂ ·6H ₂ O (0.25 mmol), NH ₂ -BTBTH ₃ (0.025 mmol) and Bipy (0.020 mmol) were dissolved in a 3 mL DMA-H ₂ O solution (v/v = 1/2), 100 °C for 48 h.	10 mg catalyst, 30 mg [Ru], 30 mL mixed solution of H ₂ O/MeCN/TIPA (v/v/v = 2/25/3), RT	300 W xenon lamp (λ ≥ 420 nm)	CO = 1326.7 μmol h ⁻¹ g ⁻¹ CO = 653.6 μmol h ⁻¹ g ⁻¹	39
Ni-BDC NNs	Thermal expansion-quench: Ni ₂ (OH) ₂ (1,4-BDC) (Ni-BDC-250); heated to 250 °C and immediately dipped it into the cryogenic liquid N ₂ (−196 °C), followed by a drastic gasification of liquid N ₂ , thus yielding NiBDC NNs	H ₂ O/MeCN/TEOA, [Ru], 30 °C, 1 atm CO ₂	visible-light irradiation (λ ≥ 400 nm)	CO = 7000 μmol h ⁻¹ g ⁻¹	69
Ni-MOF	Hydrothermal: Ni-MOF: leachate Ni, NDT (100 mg), 65 °C for 12 h	1 mg catalyst, 7.5 mg [Ru], 2 mL water, 3.0 mL MeCN, 1 mL TEOA, RT, atmospheric pressure	5 W bright LED irradiation (400–1000 nm)	CO = 13600 μmol h ⁻¹ g ⁻¹	75
Ni-SA	Hydrothermal: H ₂ O, Nickel chloride and succinic acid	MeCN/water (v/v, 4:1), TEOA, [Ru]	LED irradiation (>410 nm)	CO = 6.960 μmol h ⁻¹ g ⁻¹	73
Ni _{0.75} Mg _{0.25} -MOF-74	Solvothermal: H ₂ DOBDC (0.75 mmol), Ni(CH ₃ COO) ₂ ·4H ₂ O (0.4 mmol), Mg(CH ₃ COO) ₂ ·4H ₂ O (1.6 mmol), H ₂ O (50 mL) and 175 °C for 12 h. Activated at 200 °C under Ar atmosphere for 8 h	3 mg catalyst, 5 mL MeCN, 1 mL TEOA at 20 °C, 7 mg [Ru]	300 W xenon lamp (λ ≥ 420 nm)	HCOO [−] = 640 μmol h ⁻¹ g ⁻¹	77
Co _{0.2} Ni _{0.8} -MOFs	Solvothermal: The synthesis of Co _{0.2} Ni _{0.8} -MOFs followed the Ni-MOF protocol, substituting Ni(NO ₃) ₂ ·6H ₂ O with a mixture of Ni(NO ₃) ₂ ·6H ₂ O and Co(NO ₃) ₂ ·6H ₂ O at molar ratios of 2:1, 1:1, and 1:2, H ₂ O/DMF mixture (15 mL, v/v = 3:1); heated at 160 °C for 4 days	2 mg catalysts, 0.43 mmol/L of [Ru], 0.3 mol/L TEOA, 5 mL MeCN/H ₂ O (v/v = 4:1)	300 W Xe lamp (λ ≥ 420 nm)	CO = 1160 μmol h ⁻¹ g ⁻¹	78
Ni/Ti Bimetallic MOFs	Hydrothermal: NH ₂ BDC (15 mmol), Ti(OC ₂ H ₅) ₄ (1.3 mL), DMF (45 mL), methanol (5 mL), Ni(NO ₃) ₂ ·6H ₂ O (0.2, 2, and 2.86 mmol. Heated at 150 °C for 20 h		xenon lamp (λ > 350 nm)	CO = 13.37 μmol h ⁻¹ g ⁻¹ CH ₄ = 0.35 μmol h ⁻¹ g ⁻¹	76
Co _{0.1} Ni _{0.9} -MOF	Hydrothermal: H ₂ O (5 mL), Ni(NO ₃) ₂ (21 μL, 1 M), diphenylalanine (40 μL), Co(NO ₃) ₂ (0.1 M), of NaOH (15 μL, 1 M). Heated at 80 °C for 24 h	10 mg of the samples, RT, 75 kPa, 0.4 mL of deionized water, 10 h	300 W Xe lamp	CO = 38.74 μmol h ⁻¹ g ⁻¹	79
Ni _{0.4} Co _{0.6} -MOF	Hydrothermal: MeCN (2 mL) and H ₂ O (6 mL), HCl (200 μL); (Ni(NO ₃) ₂ ·6H ₂ O, Ni(NO ₃) ₂ ·6H ₂ O and Co(NO ₃) ₂ ·6H ₂ O were employed in a molar ratio of 1:9–9:1). Heated to 130 °C for 24 h	1 mg of catalyst, 50 mg BiH ₃ , 5 mL MeCN, 1 mL H ₂ O	300 W Xe lamp	CO = 9100 μmol h ⁻¹ g ⁻¹	83

Table 2. continued

Photocatalyst	Synthesis of MOF	Feed composition	Light source	Product	Ref
Co/Ni-MOF-741	Hydrothermal: DHTA (0.08 g), H ₂ O (12.5 mL), anhydrous ethanol (25 mL), (CH ₃ COO) ₂ Co·4H ₂ O (0.125 g) and Ni(CH ₃ COO) ₂ ·4H ₂ O (0.125 g). Heated at 120 °C for 12 h.	2 mg of catalyst, [Ru], TEOA	300 W xenon lamp ($\lambda \geq 420$ nm)	CO = 4539 $\mu\text{mol h}^{-1} \text{g}^{-1}$	84
Ni-Ni-MOL	Hydrothermal: DMF (15 mL), H ₂ O (2 mL), NaOH (0.08 mmol) naphthalene-2,6-dicarboxylic acid (1.0 mmol), Ni(NO ₃) ₂ ·6H ₂ O (1.3 mmol). Heated at 120 °C for 24 h	1 mg of catalyst, 0.2 mL TEOA, 2 mg [Ru], 1 mL H ₂ O and MeCN; for 18 h at RT	300 W xenon lamp with a filter ($\lambda \geq 420$ nm)	CO = 2400000 $\mu\text{mol g}^{-1}$ for 18 h	80
NiZrCu-BDC	Ultrasonication: H ₂ BDC (124.6 mg) in DMF/EtOH (32:2 mL); Ni(NO ₃) ₂ ·6H ₂ O, ZrCl ₄ , Cu(NO ₃) ₂ ·3H ₂ O added with TEA (0.8 mL), N ₂ purged, sonicated 8 h. Product washed with EtOH and dried at 60 °C	20 mg of catalyst, 15 mL of MeCN, 5 mL of deionized water	300 W Xe lamp	CH ₄ = 41.05 $\mu\text{mol h}^{-1} \text{g}^{-1}$ CH ₃ OH = 36.62 $\mu\text{mol h}^{-1} \text{g}^{-1}$	81
Fe/Ni-MOF-T120	Solvothermal: FeCl ₃ ·6H ₂ O (0.7892 g) and Ni(NO ₃) ₂ ·6H ₂ O (0.4214 g) coadded in Fe-MOF synthesis; reactions performed at varying temperatures (80–180 °C) and times (10–20 h)	0.5 mg of photocatalyst [Ru(bpy) ₃]Cl ₂ ·6H ₂ O (10 mg), H ₂ O (10 mL), TEOA (10 mL), and MeCN (40 mL)	300 W xenon lamp with a UV cutoff filter (CUT 420 nm)	CO = 9740 $\mu\text{mol h}^{-1} \text{g}^{-1}$	82
30%-Cu ₂ O/Ni-MOF	Solvothermal: • Ni-MOF: Ethanol (4 mL), DMF (64 mL), water (4 mL), H ₂ BDC (0.25 g) and NiCl ₂ ·0.6 H ₂ O (0.36 g). Heated at 140 °C for 24 h • 30%-Cu ₂ O/Ni-MOF: Ni-MOF (0.1 g), water (20 mL) NaOH (80 mg), 0.5 mmol Cu ₂ SO ₄ ·5H ₂ O, L-ascorbic acid (176 mg)	20 °C, 20 mg of photocatalyst, 4 h	xenon lamp	CO = 21.7 $\mu\text{mol h}^{-1}$ (after 4 h)	100
TiO ₂ @CoNi-MOF	Solvothermal: Co(NO ₃) ₂ ·6H ₂ O (0.026 mmol) and Ni(NO ₃) ₂ ·6H ₂ O (0.026 mmol), 2-methylimidazole (0.9 mmol) methanol (15 mL). Heated at 120 °C for 2 h	5 mg of the sample, RT, 1 h	300 W xenon lamp	CH ₄ = 41.65 $\mu\text{mol h}^{-1} \text{g}^{-1}$ CO = 16 $\mu\text{mol h}^{-1} \text{g}^{-1}$	101
MOF-808-CuNi	Solvothermal: H ₂ BTC and ZrOCl ₂ ·8H ₂ O, solvent mixture of DMF/formic acid, of Ni(NO ₃) ₂ ·6H ₂ O (10 mg) and 8 mg of Cu(NO ₃) ₂ ·3H ₂ O (10 mg). Heated at 135 °C for 48 h	25 mg of photocatalyst, 50 mg of [Ru], 10 mL of TEOA, 10 mL of H ₂ O	300 W Xe lamp (420 nm < λ < 760 nm)	CH ₄ = 158.7 $\mu\text{mol h}^{-1} \text{g}^{-1}$	102
NiO/Ni-BDC	Solvothermal: H ₂ BDC (1.0 mmol), DMF (15 mL), NiO (100) (3.3 mmol), NaOH (0.8 mmol). Heated at 120 °C for 2 h	5 mg of catalyst, 4.9 mL MeCN, 0.1 mL H ₂ O, 1 h, RT	300 W Xe-lamp	CH ₄ = 21.32 $\mu\text{mol h}^{-1} \text{g}^{-1}$	104
Cs ₂ AgBiBr ₆ /Ni-MOF	Ultrasonic-assisted synthesis: Ni-MOF NPs prepared by mixing BDC, NiCl ₂ ·6H ₂ O, and TEA in DMF/EtOH/H ₂ O, ultrasonicated 8 h, then dried	15 mg of photocatalyst and 10 mL of dried ethyl acetate, RT	300 W Xe lamp	CO = 58.85 $\mu\text{mol h}^{-1} \text{g}^{-1}$	110
CdS/Ni-MOF	Self-assembly: Cs ₂ AgBiBr ₆ /Ni-MOF hybrids formed by dispersing Ni-MOF in EA, adding CABB, stirring 10 h, then drying. Hybrids denoted as 0.3CABB/Ni-MOF, 0.4CABB/Ni-MOF, and 0.5CABB/Ni-MOF Solvothermal: • Ni-MOF: DMF (4 mL), ethanol (4 mL) and water (4 mL), H ₂ BDC (1.5 mmol), NiCl ₂ ·6H ₂ O (1.5 mmol). Heated at 140 °C for 24 h • 20%-CdS/Ni-MOF: 0.1 g of Ni-MOF, Cd(CH ₃ COO) ₂ ·2H ₂ O (48 mg), thiocetamide (13.8 mg), water (40 mL). Heated at 80 °C for 2 h	50 mg of catalyst, 4 h, RT	300 W xenon lamp	CH ₄ = 15.43 $\mu\text{mol h}^{-1} \text{g}^{-1}$ CO reached 7.47 $\mu\text{mol g}^{-1}$ in the fourth hour	105
Ni(OH) ₂ -4/PB	Synthesis of NMF/CPB-NCs Hot-injection: Cs ₂ CO ₃ (0.625 mmol), OA (2 mmol), and ODE (10 mL); degassed at 120 °C for 1 h, then heated to 150 °C to form Cs-oleate. PbBr ₂ (1.38 mg) in ODE (10 mL), OA (1 mL), OAm (1 mL); degassed at 120 °C, then heated to 170 °C under N ₂ . Cs-oleate (0.8 mL) rapidly injected; quenched after 5 s. Product collected by centrifugation and redispersed in toluene Hydrothermal: PB nanofibers (30 mg) dispersed in H ₂ O with hexamethylenetetramine, trisodium citrate, and Ni(NO ₃) ₂ ·6H ₂ O. Heated at 90 °C for 6 h. Product (Ni(OH) ₂ -x/PB) centrifuged, washed, and dried at 80 °C	5 mg of catalyst, ethyl acetate/water solution (5 mL, 49:1, v/v), 4 h, RT	00 W Xe lamp (420 < λ < 780 nm)	CO = 50.7 $\mu\text{mol h}^{-1} \text{g}^{-1}$ CO = 30.2 $\mu\text{mol h}^{-1} \text{g}^{-1}$ CO = 81.0 $\mu\text{mol h}^{-1} \text{g}^{-1}$	109
Pt/Ni-MOF	Solvothermal: Ni(NO ₃) ₂ ·6H ₂ O and H ₃ bpt (2:1 molar ratio) in DMF/H ₂ O; heated at 130 °C for 60 h. Pt-loaded samples prepared by adding H ₂ PtCl ₆ ·6H ₂ O (3–9 mg); Pt content confirmed by ICP-MS (0.44–1.49%). All samples activated by CH ₂ Cl ₂ exchange (48 h) and vacuum treatment at 120 °C	1 or 0.05 mg of catalyst, 8 mg of [Ru], mixed solvent (6 mL) of 3:2:1 v/v MeCN/H ₂ O/TEOA	300 W xenon lamp ($\lambda > 420$ nm)	CO = 108800 $\mu\text{mol h}^{-1} \text{g}^{-1}$	111
CQDs-2S/Ni-MOFv	Solvothermal: NiCl ₂ ·6H ₂ O, BDC, NH ₄ Cl, and CQDs (10–75 μL) in H ₂ O/EtOH/DMF; ultrasonicated, stirred, then heated at 140 °C for 24 h. Washed and vacuum-dried at 60 °C. Products labeled CQDs-X/NiMOFv	160 °C	420 nm LED	CO = 348 $\mu\text{mol h}^{-1} \text{g}^{-1}$ CH ₄ = 6 $\mu\text{mol h}^{-1} \text{g}^{-1}$	106
		5 mg of catalyst, 15 mg of [Ru], mixed solvent (6 mL) of 3:2:1 v/v MeCN/H ₂ O/TEOA	300 W xenon lamp ($\lambda > 420$ nm)	CH ₄ = 1000 $\mu\text{mol h}^{-1} \text{g}^{-1}$	112

*RT = room temperature; [Ru] = [Ru(bpy)₃]Cl₂·6H₂O (bpy = 2',2'-bipyridine); TEOA = triethanolamine; MeCN = acetonitrile; TIPA = triisopropanolamine; BIH = 1,3-dimethyl-2-phenyl-2,3-dihydro-1H-benzo[d]imidazole.

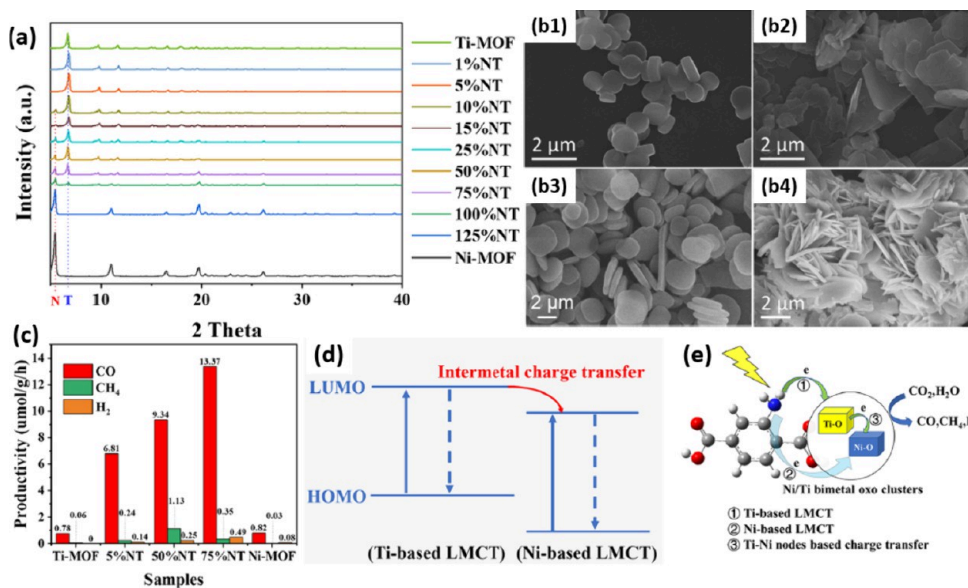


Figure 10. (a) XRD patterns of the samples. (b) SEM images: (b1) Ti-MOF, (b2) Ni-MOF, (b3) 5%NT, (b4) 75%NT. (c) Photocatalytic performance. (d) Photogenerated charge transfer diagram. (e) Electron transfer reaction scheme. Reproduced with permission from ref 76. Copyright 2021 American Chemical Society.

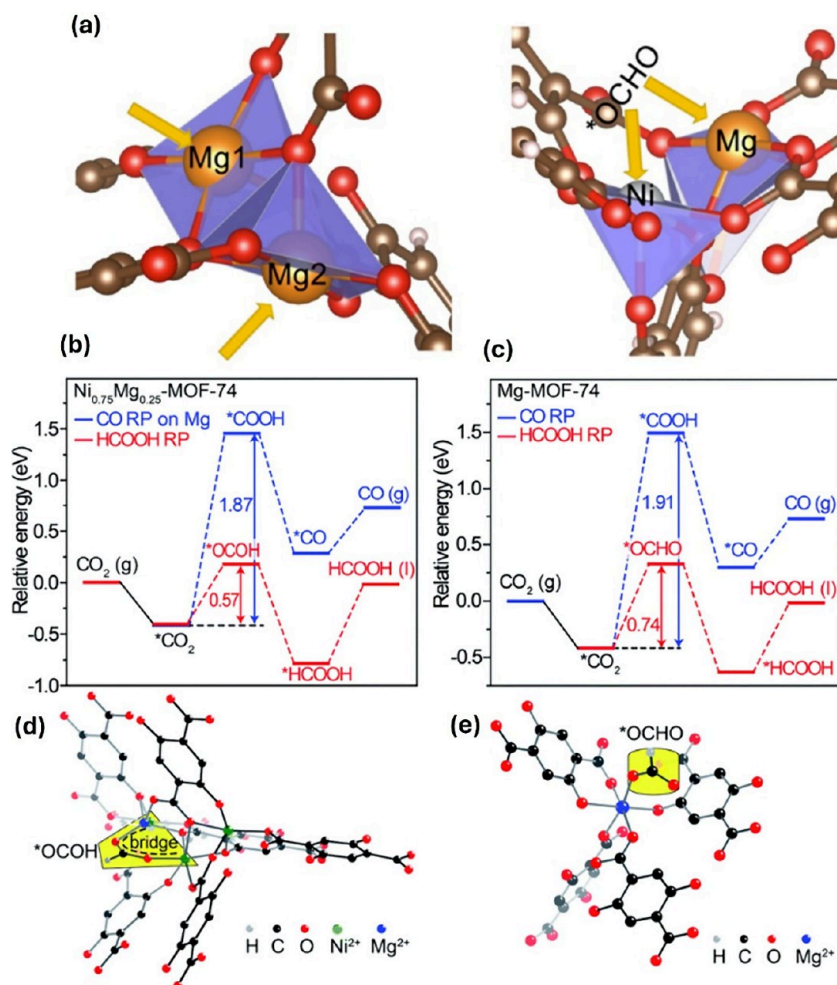


Figure 11. Geometry structures of monometallic Mg-MOF-74 (left side) and mixed Ni–Mg framework in polyhedral style (a). Calculated energy diagram for CO₂ photoreduction based on (b) Ni_{0.75}Mg_{0.25}-MOF-74 and (c) Mg-MOF-74. (d) The calculated *OCHO adsorption structure on Ni_{0.75}Mg_{0.25}-MOF-74 with a bridge structure (note: the dotted line serves as a guide to the eye). (e) Configuration of *OCHO adsorbed on Mg-MOF-74. Reproduced with permission from ref 77. Copyright 2020 Royal Society of Chemistry.

Another representative example that demonstrates the impact of bimetallic MOFs on photocatalytic capabilities is the use of a bimetallic Ni/Mg-MOF-74 photocatalyst of CO₂ to format with different ratios of Ni/Mg.⁷⁷ Ni_{0.75}Mg_{0.25}-MOF-74 achieves a production yield of 640 $\mu\text{mol h}^{-1} \text{g}^{-1}$, which exceeds that of Ni-MOF-74 (290 $\mu\text{mol h}^{-1} \text{g}^{-1}$) and Ni_{0.87}Mg_{0.13}-MOF-74 (540 $\mu\text{mol h}^{-1} \text{g}^{-1}$). In contrast, the monometallic Mg-MOF-74 shows minimal activity, suggesting that the reactivity hinges on the metal sites and the synergy between metals within the MOFs. As shown in Figure 11a, the Mg1 and Mg2 sites in the monometallic Mg-MOF-74 structure are oriented in distinct planes and directions, suggesting that the formation of a bridging structure on this framework is unlikely. However, to better understand the enhanced photocatalytic CO₂ reduction performance of bimetallic Ni/Mg-MOF-74, DFT calculations were carried out (Figure 11). The results indicate that CO and HCOOH are generated via distinct intermediates *COOH and *OCHO, respectively, each with different bonding configurations to the active sites.⁷⁷ Notably, the initial protonation step is identified as the rate-determining step. The calculations reveal that CO₂ exhibits a much stronger adsorption affinity for Mg sites (−0.41 eV) compared to Ni sites (−0.08 eV), suggesting that CO₂ activation is more likely to occur at Mg centers, which may account for the improved activity of the Ni/Mg-MOF-74 system.

The same strategy was applied by adding Co to the Ni-MOF with different ratios of Co/Ni.⁷⁸ The optimized bimetallic Co₁Ni₂-MOF displayed a superior photocatalytic efficiency in CO₂-to-CO transformation, with a production yield of 1160 $\mu\text{mol g}^{-1} \text{h}^{-1}$ and a strong selectivity of 94.6%, outperforming monometallic Co-MOF and Ni-MOF. The replacement of 4,5-dicarboxylic acid and 4,4'-bipyridine ligands with 2,2'-bipyridine-5,5'-dicarboxylic acid ligand led to another bimetallic Ni–Co-based MOF that yields 17600 $\mu\text{mol g}^{-1} \text{h}^{-1}$.⁸³ The employment of 2,5-dihydroxyterephthalic acid as a ligand in another investigation on Ni-Co-MOF results in a production rate of 4539 μmol of CO.⁸⁴

When this Co-doped effect was associated with the impact of polarization by preparing a series of Ni-MOFs with different Co-doped contents, it was demonstrated to be the driving force behind the increase in the charge separation of the MOFs. Indeed, the optimized Co_{0.1}Ni_{0.9}-MOF material showed the best CO₂ reduction achievement to CO of 38.74 $\mu\text{mol g}^{-1} \text{h}^{-1}$ under solar light irradiation beside good selectivity (almost 100%) for CO₂ reduction to CO.⁷⁹

As mentioned above for the pristine MOFs, transforming the bulk bimetallic MOF into a 2D layered material was demonstrated to enhance the photocatalytic effectiveness. Thus, this approach was also extended to bimetallic MOFs. For example, the use of 2D metal–organic layers (MOLs) based on nickel, and/or cobalt linked with bidentate ligand 2,2'-bipyridine-5,5'-dicarboxylate (H₂bpydc) (named Ni-Ni-MOL and Ni-Co-MOL) was examined for the photoreduction of CO₂ and subsequently compared their photocatalytic efficiency of CO₂ reduction to a bulky MOF with two catalytic sites (Ni-Ni-MOF) as depicted in Figure 12.⁸⁰ The ultrathin Ni-Ni-MOL or Ni-Co-MOL with two active sites displayed a considerable CO amount of 19000 $\mu\text{mol g}^{-1}$ and a high CO selectivity of 94%, which is better compared to Ni-MOL having a single catalytic site. In contrast, it was found that the CO yield decreased to 5800 $\mu\text{mol/g}$ with a CO selectivity of 91% under identical conditions using bulky Ni-Ni-MOF.⁸⁰

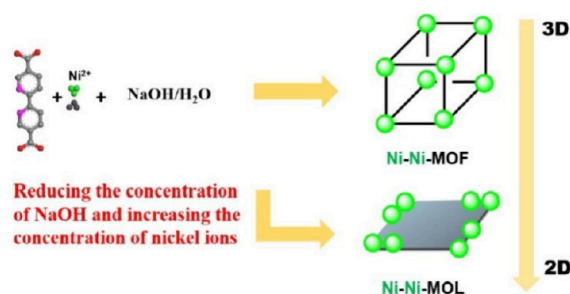


Figure 12. Diagrammatic representation of the synthesis of 2D Ni-Ni-MOL and bulky Ni-Ni-MOF. Reproduced with permission from ref 80. Copyright 2022 Wiley.

On the other hand, it was identified that the utilization of bimetallic Co/Ni-MOF enhances the process of metal–ligand–metal charge transfer (MLMCT),⁸⁵ contributing thus to the enhanced photocatalytic transformation of CO₂ to CO. To finely tune the Co metal clusters within Co-MOF-74, Ni²⁺ was implemented as a secondary metal to synthesize bimetallic Co/Ni-MOF-74-*x* (*x* = 1, 2, 3) with customizable morphology and metal ratios. The incorporation of Ni²⁺ serves a dual purpose: not only does it enhance the morphology and accentuating the rose-motif but it also significantly amplifies the specific surface area of the bimetallic rose-like Co/Ni-MOF-74-1 to an impressive 790.973 cm²/g, surpassing the monometallic rose-like Co-MOF-74 at 204.999 cm²/g. Additionally, the introduction of Ni²⁺ leads to a reduction in the band gap from 1.65 eV in Co/Ni-MOF-74-2 to 1.4 eV in Co/Ni-MOF-74-1. Experimental results from photocatalytic tests demonstrate that bimetallic Co/Ni-MOF-74-*x* (*x* = 1, 2, 3) significantly enhances the rate of CO₂ transformation. The series of bimetallic rose-like Co/Ni-MOF-74-*x* catalysts exhibit superior CO formation capabilities compared to the monometallic rose-like Co-MOF-74. Among these catalysts, bimetallic rose-like Co/Ni-MOF-74-1 achieves the highest peak CO formation rate of 4539 $\mu\text{mol g}^{-1} \text{h}^{-1}$.⁸⁵

Another strategy involves adding a third metal to the structure, which can further increase the photocatalytic activities of MOF-based photocatalysts (Figure 13).^{86,87} Figure 13a illustrates the ultrasonic-assisted synthesis of a trimetallic NiZrCu-BDC MOF. In this context, the thin trimetallic MOF based on Ni, Zr, and Cu (NiZrCu-BDC) was applied as a photocatalyst to reduce CO₂ to methanol (41.05 $\mu\text{mol h}^{-1} \text{g}^{-1}$) and ethanol (36.62 $\mu\text{mol h}^{-1} \text{g}^{-1}$) (Figure 13b). The incorporation of Zr and Cu into Ni-BDC MOF results in an increase in the surface charge density at Ni sites, which effectively enhances the chemisorption of CO₂.⁸¹ DFT calculations revealed that the enhanced CO₂ reduction activity and methanol selectivity of NiZrCu-BDC are mainly due to electron-rich Ni sites, which show stronger CO₂ adsorption and lower energy barriers for the key reaction steps. These Ni sites favor the conversion of CO* intermediates into methanol rather than allowing them to desorb. At the same time, the high energy barrier for hydrogen evolution (H₂) indicates that side reactions are effectively suppressed, which contributes to the high selectivity toward methanol.

In brief, although only a few works on mixed-metal-based photocatalysts have been reported, the combination has been found to show interesting performance in CO₂ conversion. The role of additional metal to Ni-MOFs such as Co, Cu, Mg, Zr, and Ti revealed an increased carrier separation efficiency, better

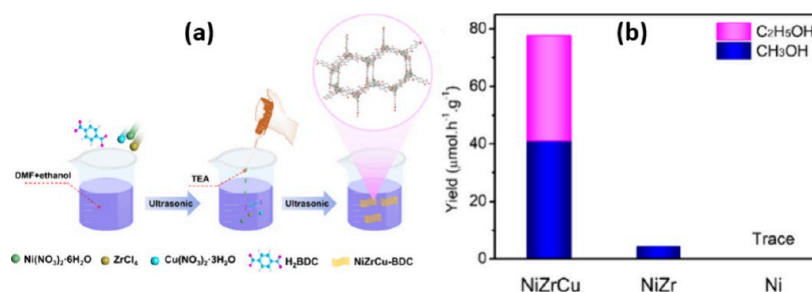


Figure 13. (a) Schematic fabrication procedure of the NiZrCu-BDC photocatalyst and (b) comparison of the formation yields of $\text{C}_2\text{H}_5\text{OH}$ and CH_3OH . Reproduced with permission from ref 81. Copyright 2022 American Chemical Society.

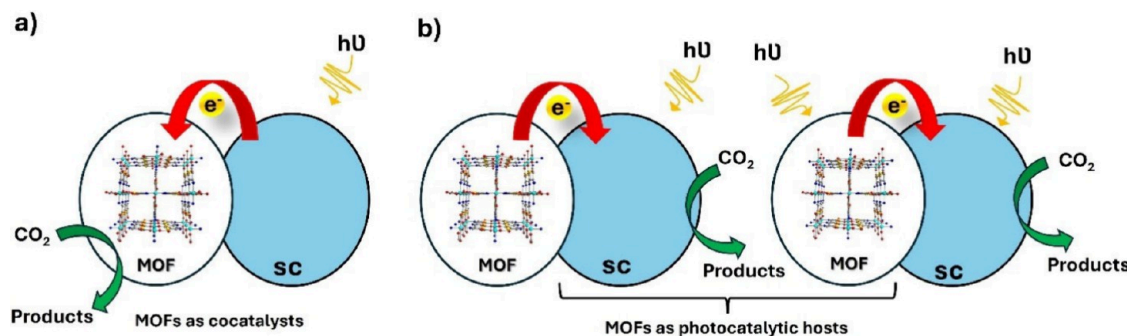


Figure 14. Schematic representations illustrating the roles of MOFs in photocatalytic CO_2 reduction: (a) as cocatalysts and (b) as photocatalytic host materials. Other photocatalytic materials are represented by blue spheres.

chemical stability, and diversity of metal-based active sites, thus improving the photocatalytic efficiency (Table 2). However, other mixed metal-based MOFs as photocatalyst materials have received limited exploration in CO_2 photoreduction up to date, and the existing literature underscored the potential and dynamic role played by Co-Ni-MOFs in photocatalysis. However, mixed metal Ni-MOFs seem to be one of the best photocatalysts for CO_2 reduction that needs more investigation and opens new perspectives in the field.

Ni-MOF Composites. Despite the intensive efforts to develop mono- or multimetallic pristine MOFs, obtaining the desired MOF-photocatalyst with high stability and outstanding catalytic activity is quite challenging. Designing MOF composites is regarded as a promising strategy to improve the catalytic effect and stability of the MOFs. Thus, MOF composites have been demonstrated to have the ability to integrate the properties of various semiconductors and the possibility to adjust their properties performance.³⁰ MOF composites offer additional utility and practicality in contrast to the bulk MOFs,⁸⁸ which allowed them to be explored in the photoreduction of CO_2 .^{30,89,90} Various semiconductors have proven to be efficient photocatalysts, like TiO_2 ,⁹¹ ZnO ,⁹² Fe_2O_3 ,⁹³ CdS ,⁹⁴ BiVO_4 ,⁹⁵ and g- C_3N_4 -based systems,⁹⁶ and so on, which can be doped into MOF systems to prepare an efficient composite. However, photoactive metal-organic frameworks (MOFs) can function either as direct photocatalysts or as supports for photocatalytic processes in the reduction of CO_2 . When exposed to light, these MOFs can absorb photons, resulting in the generation of charge carriers, electrons and holes, that drive reduction and oxidation reactions. It is important to note, however, that not all MOFs exhibit photoactivity and, even among photoactive MOFs, their semiconductor behavior differs fundamentally from that of traditional inorganic semiconductors.⁹⁷ Alternatively, MOFs can function as cocatalysts in combination with other semi-

conducting materials, as shown in Figure 14a. In this configuration, the primary light absorption and photoexcitation occur in the adjacent semiconductor (represented by the blue sphere), which transfers photogenerated electrons to the MOF. The MOF then facilitates the reduction of CO_2 using these transferred electrons. This cocatalyst system improves charge separation, prolongs carrier lifetime, and enhances selectivity by providing unique catalytic environments at the MOF interface.⁹⁸ A third configuration involves the use of MOFs as photocatalytic hosts, as depicted in Figure 14b. In this role, MOFs serve as a structural matrix that supports or encapsulates active photocatalytic components. While the semiconductor within or adjacent to the MOF performs light absorption and charge generation, the MOF contributes by adsorbing CO_2 , promoting charge transport, and enhancing the stability of the catalytic system. This synergistic interaction enables improved photocatalytic efficiency and opens pathways for designing hybrid MOF-based photocatalysts tailored for CO_2 conversion.⁹⁹

For example, Cu_2O , known as one of the good semiconductors, was used to prepare $\text{Cu}_2\text{O}/\text{Ni-MOF}$ composites to inhibit the agglomeration of the catalyst. In this work, the photocatalytic reduction of CO_2 was improved by 30% when using $\text{Cu}_2\text{O}/\text{Ni-MOF}$ ($21.7 \mu\text{mol/g}$) compared to Cu_2O ($5.32 \mu\text{mol/g}$) and Ni-MOF ($1.95 \mu\text{mol/g}$).¹⁰⁰ The photocatalytic of bimetallic MOF Co-Ni-MOF was also improved by the addition of titanium dioxide in other examples;¹⁰¹ the obtained $\text{TiO}_2@$ Co-Ni-MOF composite after optimizing the incorporated TiO_2 amount into the pore of bimetallic Co-Ni-MOF was investigated to reduce CO_2 into methane. The optimized composite photocatalyst showed significantly increased CO_2 photoreduction activity ($\text{CH}_4 = 41.65 \mu\text{mol g}^{-1} \text{h}^{-1}$) with a high CH_4 production and selectivity (93.2%) compared to single TiO_2 , pristine bimetallic Co-Ni-MOF, $\text{TiO}_2@$ Ni-MOF, and $\text{TiO}_2@$ Co-MOF. The high selectivity and/or absence of additional byproducts or impurities in the $\text{TiO}_2@$ CoNi-MOF

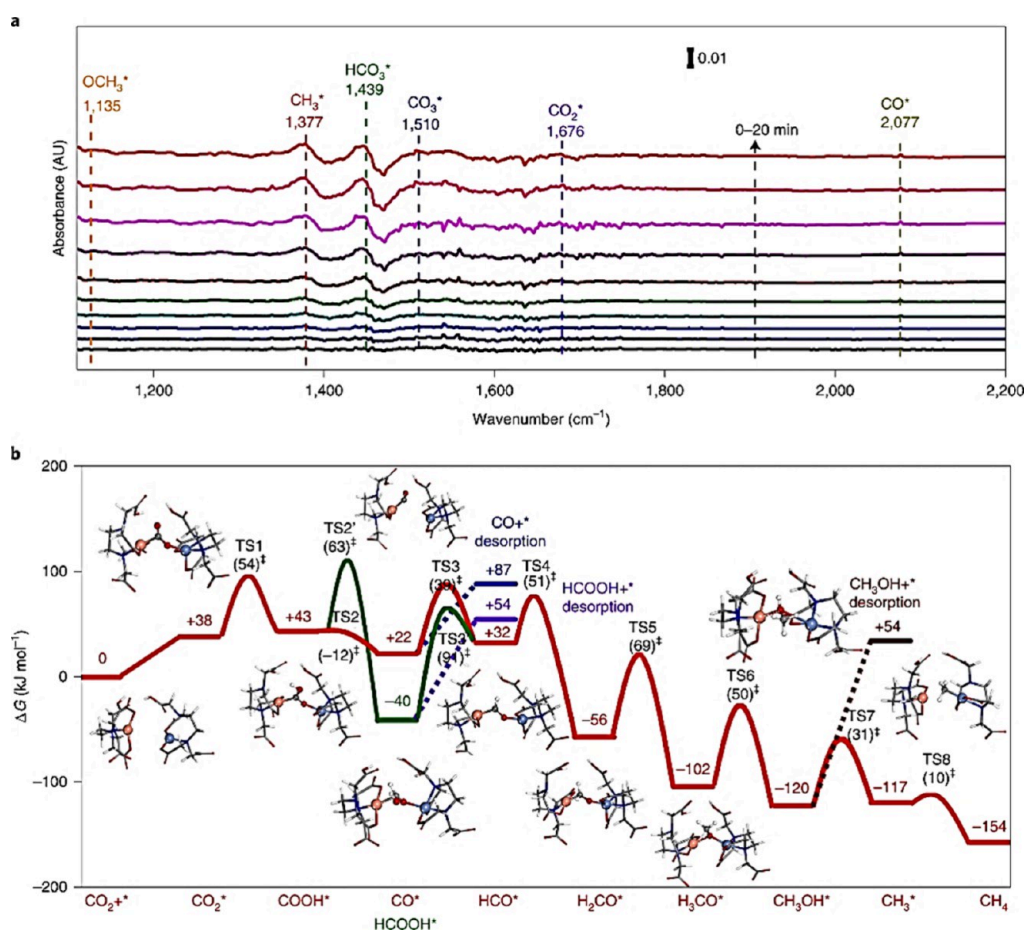


Figure 15. (a) In situ DRIFTS spectra at 1,110–2,200 cm^{-1} for detecting the reaction intermediates in CO_2 photoreduction and recording the adsorption and activation of CO_2 over MOF-808-CuNi in the presence of H_2O under visible light irradiation. AU, arbitrary units. (b) Gibbs free energy diagram. The energy data (in red) are the energy of each intermediate state, which is relative to the energy (zero) of the reference system, that is, MOF-808-CuNi and gaseous CO_2 . The energy data in parentheses (in black) are the calculated Gibbs free energy of activation for each elementary step. Reproduced with permission from ref 102. Copyright 2021 The Authors.

photocatalytic system is mainly due to the efficient charge separation and directional charge transfer enabled by the S-scheme heterojunction. This configuration ensures that only the highly oxidative holes in TiO_2 and the highly reductive electrons in CoNi-MOF participate in the reaction, minimizing unwanted side reactions. Additionally, the matched redox potentials and formation of key intermediates (such as COO^* , CHO^* , and CH_3O^*) guide the selectivity toward CH_4 and CO without forming undesired compounds. These results show the advantage and the efficiency of Ni-MOF composite for an enhanced photoreduction of CO_2 to CH_4 .¹⁰¹

In another way, and inspired by biophotocatalysts, flexible dual-metal-site pairs (DMSPs) were prepared by incorporating Ni and Cu in the MOF-808 to afford a CuNi-MOF-808 composite. This significantly increased the photocatalytic activity of CO_2 to CH_4 , resulting in a production rate of $158.7 \mu\text{mol g}^{-1} \text{h}^{-1}$ and selectivity up to 97.5%.¹⁰² The exceptional CH_4 selectivity achieved in MOF-808-CuNi stems from the synergistic effect between adjacent Cu and Ni dual-metal single sites (DMSPs), which is not observed in physical mixtures or isolated metal-functionalized MOFs. Density Functional Theory (DFT) calculations confirm that the photoreduction of CO_2 over MOF-808-CuNi follows a COOH^* intermediate pathway, which is both thermodynamically and kinetically favored over the HCOOH^* route. While HCOOH formation is

exergonic, it involves a high activation barrier and difficult desorption, redirecting the pathway toward CH_4 via key intermediates like CO^* , HCO^* , and CH_3OH^* . In contrast, MOF-808-Ni predominantly yields HCOOH due to the spontaneous desorption of HCOOH^* , while MOF-808-Cu forms CH_4 but with lower efficiency due to a higher energy barrier for CO_2 activation. These findings, supported by in situ DRIFTS and isotope labeling (Figure 15), underline how tailored electronic structures and metal-site proximity significantly influence product selectivity in MOF-based photocatalysts.¹⁰²

Heterojunction engineering is a well-established strategy to enhance the charge carrier separation and photocatalytic performance of semiconductor photocatalysts. The construction of effective interface connections to facilitate charge migration across interfaces is crucial for creating high-performance heterojunctions.¹⁰³ A series of sequence-bonded homologous heterojunction photocatalysts was designed in this context, specifically NiO(111)/Ni-BDC prepared by H_2BDC in situ etching octahedral Nickel oxide.¹⁰⁴ These photocatalysts were fabricated through in situ etching of octahedral NiO(111) using H_2BDC and were employed for the photocatalytic reduction of CO_2 (pCO_2RR) into CH_4 and CO . The facet-dependent performance of NiO in NiO/Ni-BDC heterojunctions underscores the importance of surface atomic arrangements in

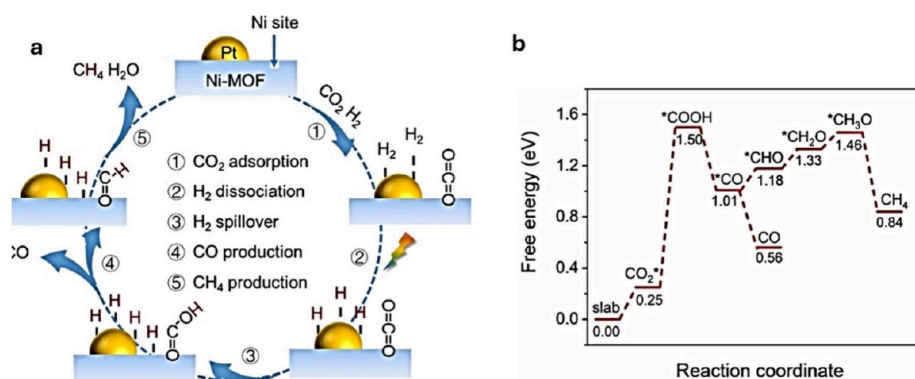


Figure 16. (a) Reaction mechanism and (b) free energy diagram of CO₂ reduction for Pt/Ni-MOF. Reproduced with permission from ref 106. Copyright 2023 Wiley.

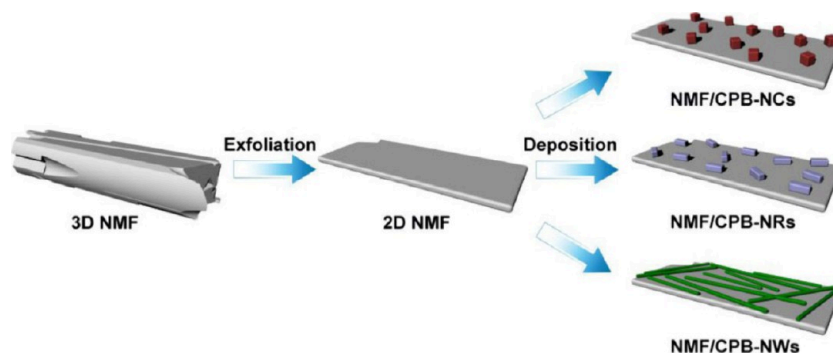


Figure 17. Diagram depicting the preparation of NMF/CPB (nanocubes, nanorods, and nanowires). Reproduced with permission from ref 109. Copyright 2021 Elsevier.

determining photocatalytic CO₂-to-CH₄ selectivity. Octahedral NiO(111)/Ni-BDC-3 exhibits a CH₄ yield (21.32 $\mu\text{mol}\cdot\text{g}^{-1}\cdot\text{h}^{-1}$) and selectivity (76.6%) far superior to its NiO(100) counterpart (6.16 $\mu\text{mol}\cdot\text{g}^{-1}\cdot\text{h}^{-1}$, 38.0%), despite their nearly identical CO₂/H₂O adsorption capacities and energetics as shown by TPD and DFT-calculated absorption energies (E_{abs}) values. These findings point to enhanced charge transfer and electron-supply dynamics as true differentiators. DFT charge density difference maps reveal that the internal electric field in NiO(111) facilitates complete Ni–O layer charge separation and efficient bulk-to-surface migration, enabling high-density electron accumulation at the interface. This theoretical insight is corroborated by photoelectrochemical and transient-state surface photovoltage experiments, demonstrating lower charge transfer resistance, longer carrier lifetimes, and greater electron flux. Thus, the unique electronic structure and charge dynamics of NiO(111) dominate the observed enhancement in CH₄ selectivity, emphasizing the crucial role of facet engineering and DFT-guided charge behavior analysis in photocatalyst design.

Sulfur-based photocatalysts, like cadmium sulfide (CdS), are widely used due to their outstanding visible light responsiveness and narrow band as semiconductor photocatalysts. Several studies have demonstrated that the photocatalytic activity of CdS composite with other semiconductor materials has been achieved.^{65,94} Doping the CdS into Ni-MOF is an ideal strategy for synthesizing CdS/Ni-MOF composite.¹⁰⁵ The optimized 20%-CdS/Ni-MOF displayed better photocatalytic efficiency than the individual Ni-MOF and CdS. It is found that the hierarchical structure of this composite avoids the clustering of

CdS and reveals additional active sites to contribute to the photoreduction reaction of CO₂.¹⁰⁵

To increase further the photocatalytic performance, and due to the known photocatalytic activity of noble metals such as palladium and platinum, they were recently explored for converting atmospheric CO₂ into useful compounds using a platinum-loaded nickel-based metal–organic framework (Pt/NiMOF).¹⁰⁶ This catalyst demonstrates exceptional activity, even when subjected to infrared light. The open nickel (Ni) sites in the MOF effectively capture and activate atmospheric CO₂, meanwhile, the platinum (Pt) sites facilitate the H₂ dissociation via photogenerated electrons. Thermal energy aids in the transfer of dissociated hydrogen to the Ni sites, where adsorbed CO₂ undergoes thermal reduction to produce CO and CH₄. Moreover, the reaction pathway for CO₂ conversion on the Ni sites of Pt/NiMOF involves several steps (Figure 16). Initially, CO₂ is captured and converted to CO via the CO₂-*COOH-*CO-CO(g) route, consistent with prior findings.^{107,108} Concurrently, some of the *CO is further hydrogenated to *CHO and quickly protonated to form *CH₃O, which then leads to the production of CH₄. This dual-active-site synergy results in Pt/NiMOF achieving a remarkable effectiveness of 9.57% at a 940 nm wavelength for transforming atmospheric CO₂. In addition, DFT studies indicate that the main bottleneck in the reduction of CO₂ over Pt/Ni-MOF is the formation of the *COOH intermediate, which requires significantly more energy than either H₂ splitting on Pt or hydrogen transfer to the Ni-MOF surface. This supports experimental data and points to a reaction mechanism where Pt primarily activates hydrogen, while Ni-MOF facilitates CO₂ conversion. This separation of active sites enhances reaction efficiency and prevents

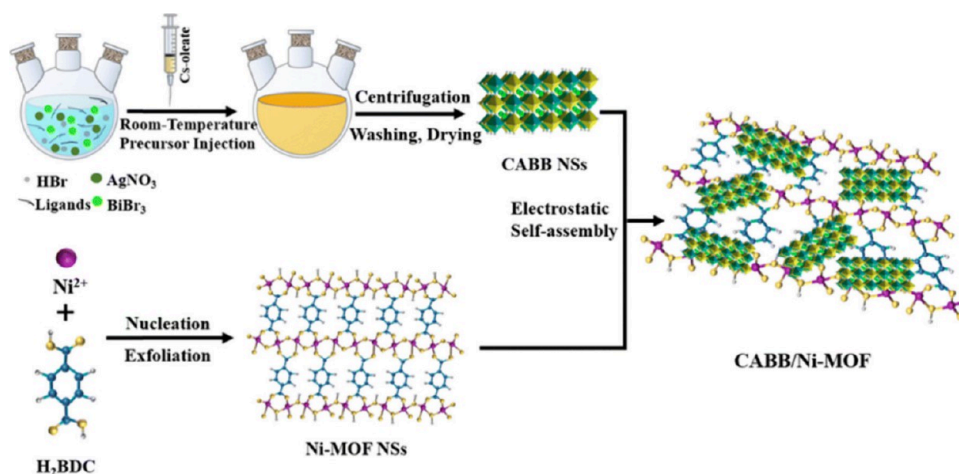


Figure 18. Diagram depicting the electrostatic self-assembly process of the 2D/2D CABB/Ni-MOF hybrid. Reproduced with permission from ref 110. Copyright 2023 Royal Society of Chemistry.

deactivation of Pt by strongly adsorbed CO. Unlike conventional photocatalytic systems, where light mainly reduces activation energy, the Pt/Ni-MOF system benefits from a combined photothermal effect that improves reaction kinetics and selectivity, yielding notably high quantum efficiencies for CO₂ conversion under mild conditions.

As discussed before in the monometallic Ni-MOF section, 2D MOF-based composites play a significant role in enhancing the photocatalytic CO₂ reduction performance. Following this, a composite of 2D Ni-MOF (NMF) and CsPbBr₃ (CPB) phases (NMF/CPB) was explored as a photocatalyst for CO₂ photoreduction to CO. The as-obtained NMF/CPB in different geometries nanocubes (NCs), nanorods (NRs) and nanowires (NWs) (Figure 17) displayed a production rate of 50.7, 30.2, and 81.0 $\mu\text{mol g}^{-1} \text{h}^{-1}$ for NMF/CPB-NCs, NMF/CPB-NRs and NMF/CPB-NWs, respectively, and recyclability up to five cycles.¹⁰⁹ Thus, investigating the 2D Ni-MOF as a photocatalyst demonstrates improved photocatalytic CO₂ reduction performance.

2D/2D perovskite/MOF hybrid was also studied for photocatalytic CO₂ reduction, fabricated through an electrostatic self-assembly process (Figure 18).¹¹⁰ This research highlights that 2D MOFs can act as effective cocatalysts to enhance the CO₂ photoreduction efficiency of perovskites when exposed to simulated solar light. Notably, the ideal CABB/Ni-MOF hybrid achieved an impressive electron consumption rate of 241.14 $\mu\text{mol g}^{-1} \text{h}^{-1}$, which is 6.43 times superior to that of pristine Cs₂AgBiBr₆ (CABB) and 8.79 times superior to that of Ni-MOF alone. The significant improvement in the photocatalytic performance of the CABB/Ni-MOF hybrid can be ascribed to several factors: the enhanced CO₂ adsorption capacity and the distinctive S-scheme heterojunction responsible for the preservation of a high reduction potential and the effective separation of charge carriers.¹¹⁰

In another way, a special class of MOF composite made from an ultrathin Ni(OH)₂ with Prussian blue (PB) was reported.¹¹¹ The PB with cyanide (–CN) groups and Fe element exhibit good electric conductivity; however, it still suffers from limited photocatalysis activity in the absence of Ni element as a decent photocatalytic active site. The addition of Ni(OH)₂ provides to Ni(OH)₂/PB photocatalyst a good performance with an efficient rate of CO evolution of 108800 $\mu\text{mol h}^{-1} \text{g}^{-1}$ and excellent selectivity (88.2–95.0%). The incorporation of carbon

quantum dots (CQDs) with an oxygen vacancy modified NiMOFs also enhances the photocatalytic activity of Ni-MOF. The optimized CQDs/NiMOF shows a production rate of 1000 $\mu\text{mol h}^{-1} \text{g}^{-1}$ for CH₄ with a high selectivity (97.58%).¹¹²

So far, composites are an ideal strategy for preparing photocatalysts for CO₂ reduction with excellent selectivity and stability relative to benchmark photocatalysts due to the collaborative effect of Ni-MOFs and the incorporated semiconductors. The effective establishment and utilization of Ni-MOF composites offer a new route for researchers in designing and developing efficient heterostructure photocatalysts for CO₂. Additionally, Table 2 provides a comparison between the different Ni-MOFs-based photocatalysts (pristine Ni-MOFs and Ni-MOF-based composites) discussed in the above sections. This table shows the specific parameters and conditions, including feed composition and light source, that can be employed with these photocatalysts to achieve the highest yield possible for the desired products such as CO, CH₄, HCOO[–], and CH₃OH.

Ni-MOF Derivatives. Despite the importance of the Ni-MOF in photocatalysis, the photocatalytic utilization of pristine MOFs is still restricted by their low conductivity, weak charge transfer, and poor stability. As an alternative, Ni-MOF-derived photocatalysts for enhanced CO₂ reduction upon thermal or chemical conversion have witnessed remarkable interest in recent years.⁵² The utilization of Ni-MOFs as templates or precursors following some heating rate, under or without a gas atmosphere, can yield stable oxides and carbonaceous materials with well-scattered active sites which are not typically found in pristine MOFs or conventional oxides or carbons.¹¹³ These derivatives-based MOFs inherit many properties of parent MOFs such as large surface area, higher porosity, and morphology, which make them promising candidates for photocatalytic applications.¹¹⁴ Particularly, the Ni-MOF derivatives including porous carbons, oxides, and their nanocomposites, mainly obtained after pyrolysis under a certain atmosphere (e.g., Ar, N₂), have been explored for the photocatalytic CO₂ reduction performance as summarized in Table 3, elucidating the sacrificial Ni-based MOF used, the synthetic method, and the desired product yield with its production rate. Therefore, several research efforts using MOF derivatives in photocatalytic CO₂ reduction have emerged in the past few years.^{115–118}

Table 3. Ni-MOF-Derived Catalysts for Photocatalytic CO₂ Reduction

Photocatalyst	MOF as precursor	Synthesis of MOF	Synthesis of Photocatalyst	Feed composition	Light source	Product	Ref
Ni@C-600	MOF-74 (Ni)	Solvothermal: DHTA (1.7 mmol) and NaOH (7.2 mmol) in 20 mL H ₂ O added to Ni(OAc) ₂ ·4H ₂ O (3.6 mmol) in 60 mL H ₂ O; stirred overnight. Product centrifuged, washed, soaked in MeOH overnight, and dried at 60 °C	Pyrolysis in N ₂	Ni@C-600 (45 mg), H ₂ /CO ₂ (4:1, 5 bar or 15 mL min ⁻¹)	300 W Xe lamp	CH ₄ = 488000 μmol h ⁻¹ g ⁻¹	119
CuNi/C	CuNiBTC	Solvothermal: H ₃ BTC, Cu ²⁺ /Ni ²⁺ (1:1) in EtOH/H ₂ O ₂ stirred, then heated at 160 °C for 10 h. CuNiBTC filtered, washed, dried (80 °C), and stored at 60 °C	Pyrolysis in N ₂	10 mg of CuNiBTC in TEOA/H ₂ O (1:4, 100 mL); ultrasonicated, sealed under CO ₂ (80 kPa)	300 W Xe lamp (λ > 700 nm, PLS-SXE 300E, PerfectLight)	CO = 11.205 μmol h ⁻¹ g ⁻¹	120
Ni/TiO ₂	Ni-Ti MOFs	Solvothermal: Terephthalic acid (3.53 g) in MeOH/DMF (6:54 mL); isopropyl titanate (2.1 mL) added, stirred, then heated at 150 °C for 16 h. Product centrifuged, soaked in MeOH (12 h), and vacuum-dried at 80 °C	pyrolysis in air	Catalyst (40 mg) tested under CO ₂ /H ₂ /He flow (10 mL/min) for photo- and thermal catalysis, with products analyzed by GC	A xenon lamp (PLS-SXE300UV, Beijing PerfectLight Technology Co. Ltd.)	CH ₄ = 271900 μmol h ⁻¹ g ⁻¹	121
ZnO/NiO	Ni-Zn MOFs	Solvothermal: Zn(NO ₃) ₂ ·6H ₂ O, H ₂ BDC, and Ni(NO ₃) ₂ ·6H ₂ O in DMAC/EtOH (50:30 mL). Heated at 180 °C for 3 h, washed, dried (50 °C)	pyrolysis in air	50 mg catalyst in 15 mL H ₂ O; CO ₂ /H ₂ O vapor generated in situ from NaHCO ₃ (84 mg) and H ₂ SO ₄ (0.2 mL, 2 M) under N ₂ atmosphere	300 W full-spectrum Xe lamp	CH ₃ OH = 1.57 μmol h ⁻¹ g ⁻¹	122
Ni@C	Ni-MOLs/MOFs	Solvothermal: BDC (0.75 mmol) and NiCl ₂ ·6H ₂ O or CoCl ₂ ·6H ₂ O (0.75 mmol) in DMF/EtOH/H ₂ O (32:2:2 mL) with Et ₃ N (0.8 mL); ultrasonicated (8 h, 40 kHz), centrifuged, washed, and freeze-dried	Pyrolysis in N ₂	Catalyst (1 mg), [Ru(bpy) ₃]Cl ₂ ·6H ₂ O (8 mg) in CH ₃ CN/H ₂ O/TEOA (3:2:1); CO ₂ purged, (301–303 K). Products analyzed by GC; ¹³ C CO ₂ tests confirmed CO source via GC-MS	300 W xenon lamp with a 420 nm	CO = 6025 ± 95 μmol h ⁻¹ g ⁻¹	123
Ni@GC	Ni-MOF	Solvothermal: Ni(NO ₃) ₂ ·6H ₂ O (197 mg) and graphite carbon (10.2 mg) in EtOH; sonicated, aged (12 h), dried (75 °C), then annealed at 600 °C (N ₂ , 1 h)	Pyrolysis in N ₂	Ni@GC (3 mg), Ru, MeCN/H ₂ O/TEOA (8:2:2 mL), CO ₂ (500 Torr), 300 W Xe (λ > 420 nm, 20 °C); GC analysis	300 W Xe lamp, λ > 420 nm.	CO = 27 μmol h ⁻¹ g ⁻¹	124
NiFe ₂ O ₄ @N/C/SnO ₂	FeNi-MOF/SnO ₂	Solution-phase deposition method: FeNi-MOF (0.2 g) and PVP (0.3 g) in HCl (0.0996 M); SnCl ₄ ·5H ₂ O (0.44 g) added, stirred 1 h. Product (FeNi-MOF/SnO ₂) washed with EtOH/H ₂ O and dried at 70 °C	Pyrolysis in air/N ₂	NiFe ₂ O ₄ @N/C/SnO ₂ of 0.5 mg photocatalyst, Ru (10 mg), H ₂ O/TEOA/MeCN (1:1:4, 60 mL), CO ₂ atmosphere, 5 °C. CO analyzed hourly by GC	300 W Xe lamp, λ > 420 nm	CO = 2057.41 μmol h ⁻¹ g ⁻¹	115

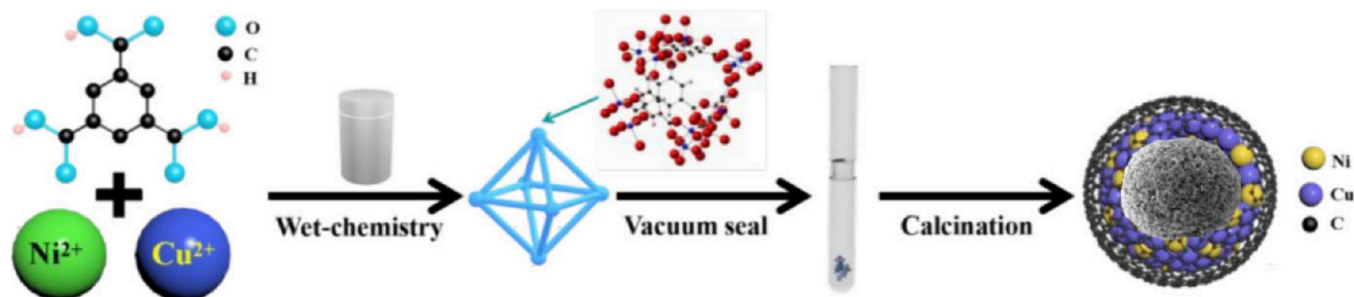


Figure 19. Representation of the Synthesis Procedure of Cu-Ni-BTC. Reproduced with permission from ref 125. Copyright 202 Royal Society of Chemistry.

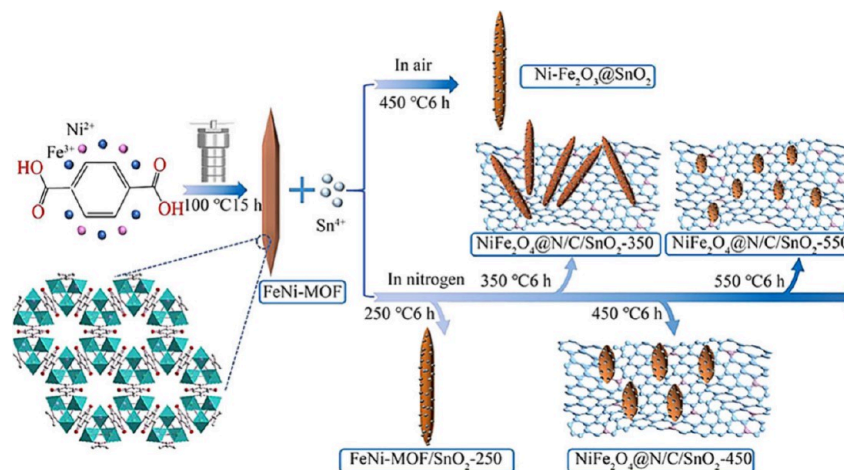


Figure 20. Methods for preparing Ni-Fe₂O₃@SnO₂ and NiFe₂O₄@N/C/SnO₂. Reproduced with permission from ref 115. Copyright 2021 Elsevier.

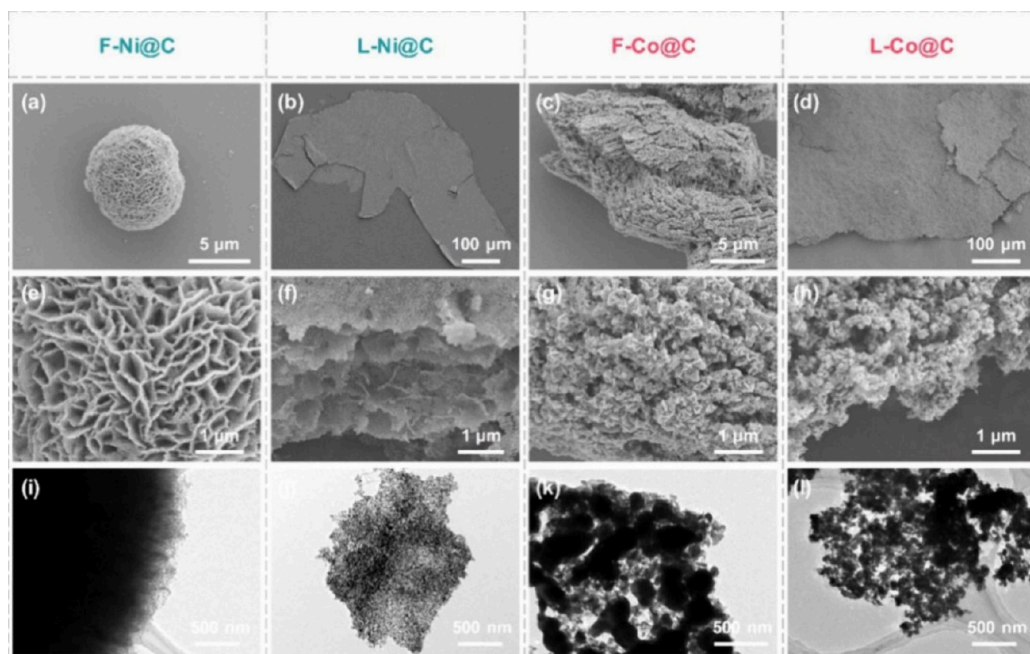


Figure 21. SEM images of the F-Ni@C (a,e), L-Ni@C (b,f), F-Co@C (c,g), and L-Co@C (d,h) samples. (i–l) TEM images of the F-Ni@C, L-Ni@C, F-Co@C, and L-Co@C samples. Reproduced with permission from ref 123. Copyright 2021 American Chemical Society.

More particularly, the treatment condition of mono or bimetallic MOFs can be controlled to form Ni encapsulated in carbonaceous structure or bimetallic oxides or metal encapsulated carbonaceous structure using bimetallic MOFs such as Cu-Ni-BTC, FeNi-MOF, and Zn-Ni MOFs. In this viewpoint, a

bimetallic MOF template was used for synthesizing carbon-coated CuNi alloy nanocatalyst (denoted as CuNi/C) through high-temperature vacuum treatment of Cu-Ni-BTC, followed by encapsulation transformed into graphitic shells using a simple in situ coating method, as shown in Figure 19. Due to the porous

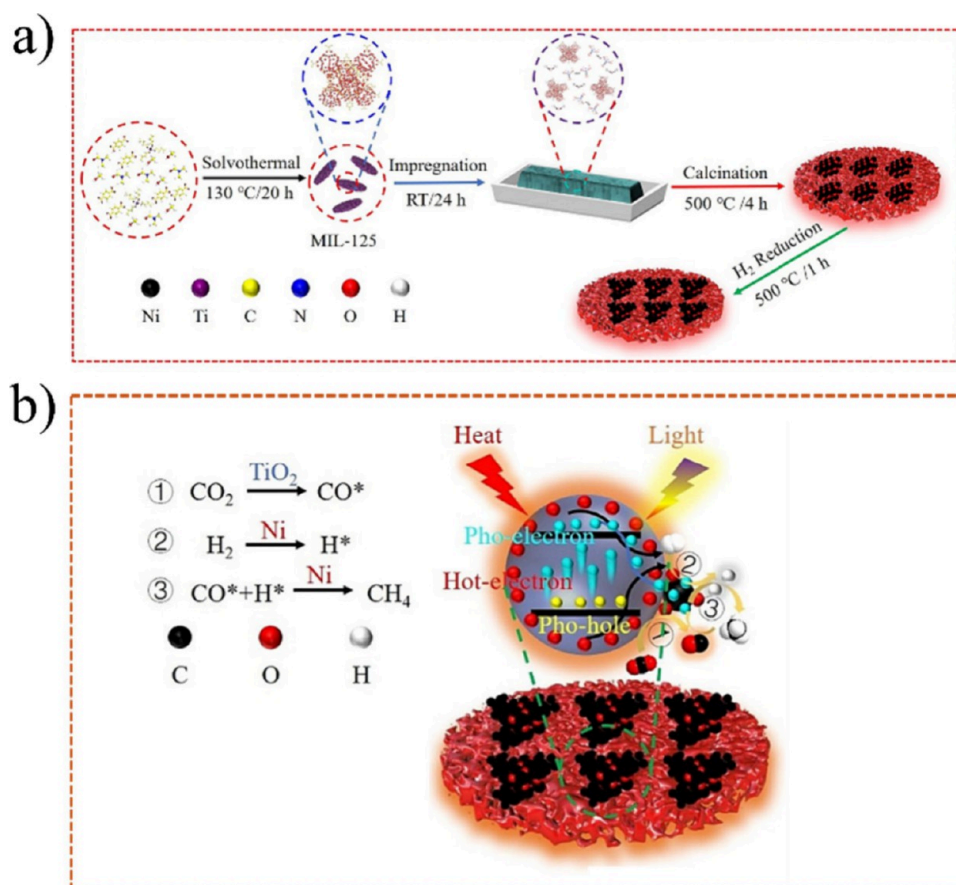


Figure 22. Preparation schemes of MIL-125 (a) and schematic of the photothermal catalytic CO₂ methanation (b). Reproduced with permission from ref 129. Copyright 2023 Elsevier.

structure inherited from CuNi-MOF, these derived catalysts demonstrate broader light absorption, greater exposure of active sites, and improved band alignment, all of which contribute to enhanced charge separation and electronic conductivity. The integration of graphene further promotes efficient transport of photogenerated electrons, facilitating charge transfer within the bimetallic photocatalysts and significantly improving their overall photocatalytic performance and selective reduction of CO₂ to CO in which the rate of precipitation of the carbon can reach 11.205 $\mu\text{mol g}^{-1} \text{h}^{-1}$. Furthermore, these photocatalysts are recyclable and stable with activity retention of 90% after a 40 h long cycle test under NIR light conditions ($\lambda > 700 \text{ nm}$), suggesting their viability for real-world applications.¹²⁰

In a similar work, as shown in Figure 20, Fe was inserted with Ni by using FeNi-MOF hybridized with Sn⁴⁺ for the synthesis of NiFe₂O₄@N/C/SnO₂ after the pyrolysis of FeNi-MOF/SnO₂ in nitrogen under different thermal treatments to prepare a variety of nanophotocatalysts NiFe₂O₄@N/C/SnO₂, which showed enhancements in addressing the low electrical conductivity of MOFs, high magnetic sensitivity and superior photocatalytic activity (2057.41 $\mu\text{mol g}^{-1} \text{h}^{-1}$) to the calcined FeNi-MOF/SnO₂, potentially attributable to the carbon–nitrogen layer formed upon postannealing, mediating the charge-transfer process.¹¹⁵

To further enhance the photocatalytic CO₂ reduction, metal–organic monolayers (MOLs) were used to compare the Ni-MOL and Co-MOL by using them as templates for the synthesis of dispersed nanoparticles of Ni@C and Co@C, respectively, through direct pyrolysis.¹²³ In this study, the as-prepared Ni@C

and Co@C nanoparticles derived Ni-MOLs and Co-MOLs, respectively, are widely spread and interconnected, resembling a sheet of paper due to an ultrathin thickness of approximately 1 nm enabling the enhanced accessibility of active metal sites (Figure 21), facilitating accelerated electron transfer from photosensitizers (Ru(bpy)³⁺) to derive Ni@C and Co@C nanoparticles during the photocatalytic CO₂ reduction. This is advantageous compared to other works where derived catalysts obtained from conventional Ni-MOFs and Co-MOFs show a three-dimensional bulk structure and agglomerated nanoparticles, wherein the most active metal sites are confined within the interior and not fully exploited in the photocatalytic CO₂ reduction reaction. Remarkably, the Ni@C derived from Ni-MOLs exhibits an increase in the CO production rate of 6025 \pm 95 $\mu\text{mol g}^{-1} \text{h}^{-1}$ under visible light irradiation ($\lambda > 420 \text{ nm}$), twice as high as that of Ni@C derived from Ni-MOFs under the identical reaction conditions. The results indicate that the MOL-derived catalysts produced a larger amount of CO than over MOF-derived counterparts. These discoveries provide valuable insights for the methodical development of catalysts derived from metal–organic frameworks (MOFs). Similarly, Lin and collaborators documented Ni nanoparticles synthesized from Ni-MOF, encapsulated within hollow spheres of few-layered graphitic carbon (Ni@GC), which exhibited excellent activity in converting CO₂ to CO, achieving a superior CO production rate of 27 $\mu\text{mol h}^{-1}$ under visible light exposure, facilitated by a ruthenium photosensitizer.¹²⁴

In another study, the MOF-based approach was utilized to fabricate ZnO/NiO porous hollow spheres that have been

successfully acquired through thermal processing of Zn-Ni MOFs acting as precursors.¹²² The synthesized porous hollow spheres of ZnO/NiO with sheet-like substructures exhibited an excellent photocatalytic performance in CO₂ reduction, and the highest CH₃OH production rate was observed which increased approximately 3-fold compared to pure ZnO, attributed to the formation of numerous p-n heterojunctions produced from the thermal decomposition of heterothallic Zn-Ni MOFs, resulting in n-type ZnO and p-type NiO.

In the realm of photothermal CO₂ methanation, Jorge Gascon and colleagues have recently published findings on highly dispersed Ni nanoparticles supported on a carbon matrix derived from Ni-MOF-74 catalyst for the photothermal reduction of CO₂ to CH₄.¹¹⁹ The photocatalyst obtained from direct pyrolysis of MOF-74 (Ni) acts as a precursor having a suitable structural and effective organization alongside an adjustable porous structure inherited from the original MOF, attaining impressive rates of conversion, selectivity, and recyclability without requiring external heating. The Ni@C catalyst leads to very high CH₄ production rates of 48800 $\mu\text{mol g}^{-1} \text{h}^{-1}$ and a selectivity of 92% after UV-vis-IR light illumination. The additional outdoor experiments of the catalysts with synthesized metal nanoparticles embedded in a carbon matrix exhibited high performance in methane production under ambient solar irradiation.

In order to achieve efficient and selective photocatalytic CO₂ reduction, researchers utilize a strategy involving MOF-derived materials with controllable defects. This approach enables the rational design of flexible hollow porous structures containing abundant defect sites and highly concentrated accessible active sites, facilitating enhanced CO₂ production efficiency and selectivity.^{121,126} This was previously achieved by designing a carbon cloth-supported flexible hollow porous array of Co-Ni spinel nanosheets with plentiful oxygen defects, enabling highly efficient and selective CO₂ photoreduction due to highly concentrated accessible active sites.¹²⁶ Thus, the synthesized hollow porous NiCo₂O₄ arrays on a carbon cloth catalyst provide a high CO yield of 19.8 μmol , high stability, and a noticeable selectivity of 95%. These findings highlight the potential of nanostructure manipulation and defect engineering to enhance the light utilization and active site accessibility for efficient CO₂ photoreduction.

This type of metal nanoparticle embedded in a carbon matrix derived from MOFs, MOF-derived porous metal oxides, brings many benefits: (i) These MOF derivatives provide highly accessible surfaces and abundant pores, promoting the exposure of numerous active sites in reactions. This reduces the transfer distance to the pore surface for photoexcited carriers, thereby enhancing light utilization efficiency and contributing to their outstanding performance in CO₂ photoconversion.^{114,127} (ii) The resulting material inherits the original structure of MOFs, while thermal treatment significantly enhances the stability and electrical conductivity of pristine MOFs as well as metal nanoparticles encapsulated in the carbon layers exhibiting the highest photoreduction rate compared to the other photocatalysts. (iii) The as-prepared derived materials take advantage of their optical properties and the degree of graphitization within the carbonaceous matrix. This enhances electron transport, broadens light absorption range, and improves CO₂ capture and photoconversion efficiency toward solar fuels. As a result, MOF-derived nanomaterials present a promising avenue for developing stable, selective photocatalysts capable of maximizing CO₂ reduction into targeted products.¹²⁸

Later, nickel nanoparticles (NPs) were impregnated into TiO₂ (Ni-TiO₂) derived from MIL-125 (Ti-based MOFs) for photothermal CO₂ methanation (Figure 22a). Under full spectrum illumination (1200 mW/cm²) at 325 °C, CO₂ conversion reached 56%, a 1.8-fold increase compared to nonirradiated conditions. Methane selectivity was nearly 99%, with a production rate of 95700 $\mu\text{mol}/(\text{g}_{\text{cat}} \cdot \text{h})$, representing a 2.7-fold enhancement under irradiation. Moreover, the catalysts exhibited exceptional stability across four testing cycles (32 h), with no activity decline. The superior catalytic performance in photothermal CO₂ methanation was attributed to the homogeneous dispersion of Ni NPs and the synergistic effect of TiO₂'s large specific surface area coupled with abundant moderate-strength alkaline sites.¹²⁹ However, understanding the mechanism behind this improvement becomes crucial. Initially, CO₂ attaches to defects on TiO₂. Upon illumination, TiO₂ photothermal conversion ability comes into play, channeling thermal and photogenerated electrons to its surface (Figure 22b). These electrons aid in decomposing CO₂ to CO*, which readily interacts with electron-rich Ni particles. Simultaneously, Ni nanoparticles facilitate H₂ dissociation into H atoms due to their high adsorption capability and promote subsequent hydrogenation of CO* intermediates.¹³⁰ The introduction of Ni markedly boosts CO₂ conversion compared to pure TiO₂, owing to Ni particle's active role in enhancing H₂ adsorption and dissociation. Whole spectrum irradiation further amplifies this process by synergizing TiO₂ photothermal and photoelectric effects, generating and transferring electrons to facilitate CO₂ decomposition. Moreover, Ni particles serve as active sites for CO* hydrogenation into CH₄.^{131,132}

Currently, various types of metal-organic frameworks (MOFs) are being explored for CO₂ photoreduction due to their exceptional CO₂ adsorption capacity, structural versatility, strong light absorption, and high photocatalytic efficiency. Among them, nickel-based MOFs (Ni-MOFs) have emerged as particularly promising candidates for CO₂ photoreduction. The excellent catalytic activity of nickel, its strong affinity for CO₂, and its relatively low cost make Ni-MOFs attractive materials for efficient CO₂ conversion under light irradiation.

This mini-review summarizes the performance of various pristine Ni-MOFs in CO₂ photoreduction and highlights strategies employed to enhance their photocatalytic activity. Special attention is given to Ni-MOF derivatives and their applications in light-driven CO₂ conversion. The tunable pore size of Ni-MOFs allows for optimized CO₂ adsorption, while functionalization can improve light-harvesting capabilities. Additionally, Ni-MOFs can be integrated with highly efficient semiconductors to further enhance their photocatalytic performance.

Ni-MOFs might represent an efficient category within materials science, particularly as photocatalytic materials for converting CO₂ into various valuable chemicals. However, the development of this type of material faces challenges manifesting in the structural lability that limits their high performance due to the contradiction between reactivity and stability; their surface area and adsorption capacity experience a significant decline upon exposure to moisture. Another obstacle in achieving effective CO₂ photoreduction is the slow kinetics involved in the multielectron CO₂ reduction half-reaction.

To address the stability limitations of Ni-based MOFs, several strategies have been developed. Incorporating robust metals such as zirconium into mixed-metal frameworks enhances structural integrity through stronger metal-ligand bonds.

Forming composites with materials such as graphene or metal oxides can improve both stability and charge separation. Converting Ni-MOFs into Ni@C or Ni/NiO composites via pyrolysis enhances the resistance to chemical degradation. Together, these approaches highlight the importance of a rational design for achieving both high photocatalytic efficiency and long-term stability.

Nevertheless, to meet the requirements of practical photocatalytic reduction of CO₂ by Ni-MOFs, several perspectives should be addressed, including:

- (i) improving strategies are needed to enhance the stability of Ni-MOFs for long-term application in photocatalytic reactions,
- (ii) selecting the structure and ligand in Ni-MOFs should be carefully designed to improve selectivity and chemical stability,
- (iii) incorporating appropriate cocatalysts by rational design of cooperative composites can significantly enhance the photocatalytic performance of Ni-MOFs for CO₂ conversion,
- (iv) utilizing Ni-MOFs and their composites as precursors for highly stable Ni-based materials through pyrolysis or high-temperature calcination can improve durability,
- (v) investigating the CO₂ photoreduction mechanism on Ni-MOF-based catalysts is essential for identifying strategies to enhance catalytic activity.

Furthermore, optimizing the preparation methods of Ni-MOFs is crucial for their large-scale production and future industrial applications. The development of cost-effective, green, and scalable synthesis strategies, such as using inexpensive ligands or recycling waste materials, will be instrumental in making Ni-MOFs more viable for practical use. Expanding large-scale manufacturing will not only facilitate implementation of CO₂ photoreduction but also provide economic benefits, reinforcing the commercial potential of Ni-MOFs in the near future.

AUTHOR INFORMATION

Corresponding Author

Samir El Hankari – Chemical and Biochemical Sciences, Green Process Engineering, Mohammed VI Polytechnic University (UM6P), Ben Guerir 43150, Morocco; orcid.org/0000-0002-9123-6857; Email: samir.elhankari@um6p.ma

Authors

Elmechdi Moumen – Chemical and Biochemical Sciences, Green Process Engineering, Mohammed VI Polytechnic University (UM6P), Ben Guerir 43150, Morocco

Khairuddin Boukayouh – Chemical and Biochemical Sciences, Green Process Engineering, Mohammed VI Polytechnic University (UM6P), Ben Guerir 43150, Morocco

Redouane Haounati – Chemical and Biochemical Sciences, Green Process Engineering, Mohammed VI Polytechnic University (UM6P), Ben Guerir 43150, Morocco

Nor Aishah Saidina Amin – Chemical Reaction Engineering Group, Faculty of Chemical and Energy Engineering, Universiti Teknologi Malaysia (UTM), Johor 81310, Malaysia; orcid.org/0000-0003-2299-9401

Wendy L. Queen – Institute of Chemical Sciences and Engineering (ISIC), École Polytechnique Fédérale de Lausanne (EPFL), CH-1051 Sion, Switzerland; orcid.org/0000-0002-8375-2341

Complete contact information is available at:
<https://pubs.acs.org/10.1021/acs.jpcllett.5c00909>

Notes

The authors declare no competing financial interest.

ACKNOWLEDGMENTS

This work was sponsored by UM6P and the Junior Faculty Development program under the UM6P – EPFL Excellence in Africa Initiative.

REFERENCES

- (1) Kabir, M.; Habiba, U. E.; Khan, W.; Shah, A.; Rahim, S.; Rios-Escalante, P. R. D. I.; Farooqi, Z.-U.-R.; Ali, L.; Shafiq, M. Climate Change Due to Increasing Concentration of Carbon Dioxide and Its Impacts on Environment in 21st Century; a Mini Review. *J. King Saud Univ. - Sci.* **2023**, 35 (5), 102693.
- (2) Ding, M.; Flaig, R. W.; Jiang, H. L.; Yaghi, O. M. Carbon Capture and Conversion Using Metal-Organic Frameworks and MOF-Based Materials. *Chem. Soc. Rev.* **2019**, 48 (10), 2783–2828.
- (3) Karve, V. V.; Espín, J.; Asgari, M.; Van Gele, S.; Oveisi, E.; Queen, W. L. N-Containing Carbons Derived from Microporous Coordination Polymers for Use in Post-Combustion Flue Gas Capture. *Adv. Funct. Mater.* **2023**, 33 (21), 2212283.
- (4) Danouche, M.; El Ghachtouli, N.; Aasfar, A.; Bennis, I.; El Arroussi, H. Pb(II)-Phycoremediation Mechanism Using Scenedesmus Obliquus: Cells Physicochemical Properties and Metabolomic Profiling. *Heliyon* **2022**, 8 (2), e08967.
- (5) Park, J. H.; Yang, J.; Kim, D.; Gim, H.; Choi, W. Y.; Lee, J. W. Review of Recent Technologies for Transforming Carbon Dioxide to Carbon Materials. *Chem. Eng. J.* **2022**, 427, 130980.
- (6) Gür, T. M. Carbon Dioxide Emissions, Capture, Storage and Utilization: Review of Materials, Processes and Technologies. *Prog. Energy Combust. Sci.* **2022**, 89, 100965.
- (7) Garba, M. D.; Usman, M.; Khan, S.; Shehzad, F.; Galadima, A.; Ehsan, M. F.; Ghanem, A. S.; Humayun, M. CO₂ towards Fuels: A Review of Catalytic Conversion of Carbon Dioxide to Hydrocarbons. *J. Environ. Chem. Eng.* **2021**, 9 (2), 104756.
- (8) Fujishima, A.; Honda, K. Electrochemical Photolysis of Water at a Semiconductor Electrode. *Nature* **1972**, 238 (5358), 37–40.
- (9) Corma, A.; Garcia, H. Zeolite-Based Photocatalysts. *Chem. Commun.* **2004**, 1443–1459.
- (10) Arora, A. K.; Jaswal, V. S.; Singh, K.; Singh, R. Applications of Metal/Mixed Metal Oxides as Photocatalyst: A Review. *Orient. J. Chem.* **2016**, 32 (4), 2035–2042.
- (11) Wang, S.; Wang, X. Photocatalytic CO₂ Reduction by CdS Promoted with a Zeolitic Imidazolate Framework. *Appl. Catal. B Environ.* **2015**, 162, 494–500.
- (12) Aggarwal, M.; Basu, S.; Shetti, N. P.; Nadagouda, M. N.; Kwon, E. E.; Park, Y. K.; Aminabhavi, T. M. Photocatalytic Carbon Dioxide Reduction: Exploring the Role of Ultrathin 2D Graphitic Carbon Nitride (g-C₃N₄). *Chem. Eng. J.* **2021**, 425, 131402.
- (13) Liu, H.; Cheng, M.; Liu, Y.; Wang, J.; Zhang, G.; Li, L.; Du, L.; Wang, G.; Yang, S.; Wang, X. Single Atoms Meet Metal-Organic Frameworks: Collaborative Efforts for Efficient Photocatalysis. *Energy Environ. Sci.* **2022**, 15 (9), 3722–3749.
- (14) Chen, J.; Abazari, R.; Adegoke, K. A.; Maxakato, N. W.; Bello, O. S.; Tahir, M.; Tasleem, S.; Sanati, S.; Kirillov, A. M.; Zhou, Y. Metal-Organic Frameworks and Derived Materials as Photocatalysts for Water Splitting and Carbon Dioxide Reduction. *Coord. Chem. Rev.* **2022**, 469, 214664.
- (15) Ait Benhamou, A.; Moumen, E.; Aqil, M.; Amine, R.; El Fallah, H.; Son, S.-B.; Boukind, S.; El Achaby, M.; El Hankari, S.; Alami, J.; Dabbi, M.; Sehaqui, H. In Situ Synthesis of Phosphate-Based CelloMOF as a Promising Separator for Li - Ion Batteries. *ACS Appl. Energy Mater.* **2025**, 8, 3379.

- (16) Moumen, E.; El Hankari, S. El. MOF-Assisted Synthesis of Mesoporous Zirconium Phosphate for Enhanced Cadmium Removal from Water. *Colloid Interface Sci. Commun.* **2023**, *52*, 100691.
- (17) Xuan, W.; Zhu, C.; Liu, Y.; Cui, Y. Mesoporous Metal-Organic Framework Materials. *Chem. Soc. Rev.* **2012**, *41* (5), 1677–1695.
- (18) Yang, S.; Karve, V. V.; Justin, A.; Kochetygov, I.; Espín, J.; Asgari, M.; Trukhina, O.; Sun, D. T.; Peng, L.; Queen, W. L. Enhancing MOF Performance through the Introduction of Polymer Guests. *Coord. Chem. Rev.* **2021**, *427*, 213525.
- (19) Sun, D. T.; Peng, L.; Reeder, W. S.; Moosavi, S. M.; Tiana, D.; Britt, D. K.; Oveisi, E.; Queen, W. L. Rapid, Selective Heavy Metal Removal from Water by a Metal-Organic Framework/Polydopamine Composite. *ACS Cent. Sci.* **2018**, *4* (3), 349–356.
- (20) Moumen, E.; Boukayouht, K.; Elmoutchou, S.; Kounbach, S.; El Hankari, S. Sustainable and Shaped Synthesis of MOF Composites Using PET Waste for Efficient Phosphate Removal. *New J. Chem.* **2024**, *48*, 2226.
- (21) So, M. C.; Wiederrecht, G. P.; Mondloch, J. E.; Hupp, J. T.; Farha, O. K. Metal-Organic Framework Materials for Light-Harvesting and Energy Transfer. *Chem. Commun.* **2015**, *51* (17), 3501–3510.
- (22) Wang, J. L.; Wang, C.; Lin, W. Metal-Organic Frameworks for Light Harvesting and Photocatalysis. *ACS Catal.* **2012**, *2* (12), 2630–2640.
- (23) Asgari, M.; Semino, R.; Schouwink, P. A.; Kochetygov, I.; Tarver, J.; Trukhina, O.; Krishna, R.; Brown, C. M.; Ceriotti, M.; Queen, W. L. Understanding How Ligand Functionalization Influences CO₂ and N₂ Adsorption in a Sodalite Metal-Organic Framework. *Chem. Mater.* **2020**, *32* (4), 1526–1536.
- (24) Justin, A.; Espín, J.; Kochetygov, I.; Asgari, M.; Trukhina, O.; Queen, W. L. A Two Step Postsynthetic Modification Strategy: Appending Short Chain Polyamines to Zn-NH₂-BDC MOF for Enhanced CO₂ Adsorption. *Inorg. Chem.* **2021**, *60* (16), 11720–11729.
- (25) Alkhatib, I. I.; Garlisi, C.; Pagliaro, M.; Al-Ali, K.; Palmisano, G. Metal-Organic Frameworks for Photocatalytic CO₂ Reduction under Visible Radiation: A Review of Strategies and Applications. *Catal. Today* **2020**, *340*, 209–224.
- (26) Wang, D.; Huang, R.; Liu, W.; Sun, D.; Li, Z. Fe-Based MOFs for Photocatalytic CO₂ Reduction: Role of Coordination Unsaturated Sites and Dual Excitation Pathways. *ACS Catal.* **2014**, *4* (12), 4254–4260.
- (27) Liu, X.; Yang, H.; Diao, Y.; He, Q.; Lu, C.; Singh, A.; Kumar, A.; Liu, J.; Lan, Q. Recent Advances in the Electrochemical Applications of Ni-Based Metal Organic Frameworks (Ni-MOFs) and Their Derivatives. *Chemosphere* **2022**, *307*, 135729.
- (28) Li, X.; Zhu, Q.-L. MOF-Based Materials for Photo- and Electrocatalytic CO₂ Reduction. *EnergyChem.* **2020**, *2* (3), 100033.
- (29) Ye, R. P.; Ding, J.; Gong, W.; Argyle, M. D.; Zhong, Q.; Wang, Y.; Russell, C. K.; Xu, Z.; Russell, A. G.; Li, Q.; Fan, M.; Yao, Y. G. CO₂ Hydrogenation to High-Value Products via Heterogeneous Catalysis. *Nat. Commun.* **2019**, *10* (1), 5698.
- (30) Sonowal, K.; Saikia, L. Metal-Organic Frameworks and Their Composites for Fuel and Chemical Production via CO₂ Conversion and Water Splitting. *RSC Adv.* **2022**, *12* (19), 11686–11707.
- (31) Xiao, J.; Zhang, T.; Wang, Q. Metal-Organic Framework Derived Single-Atom Catalysts for CO₂ Conversion to Methanol. *Curr. Opin. Green Sustain. Chem.* **2022**, *37*, 100660.
- (32) Gao, C.; Low, J.; Long, R.; Kong, T.; Zhu, J.; Xiong, Y. Heterogeneous Single-Atom Photocatalysts: Fundamentals and Applications. *Chem. Rev.* **2020**, *120* (21), 12175–12216.
- (33) Li, X.; Yu, J.; Jaroniec, M.; Chen, X. Cocatalysts for Selective Photoreduction of CO₂ into Solar Fuels. *Chem. Rev.* **2019**, *119* (6), 3962–4179.
- (34) Guo, J.; Wan, Y.; Zhu, Y.; Zhao, M.; Tang, Z. Advanced Photocatalysts Based on Metal Nanoparticle/Metal-Organic Framework Composites. *Nano Res.* **2021**, *14* (7), 2037–2052.
- (35) Ikreedeeh, R. R.; Tahir, M. A Critical Review in Recent Developments of Metal-Organic-Frameworks (MOFs) with Band Engineering Alteration for Photocatalytic CO₂ reduction to Solar Fuels. *J. CO₂ Util.* **2021**, *43*, 101381.
- (36) Zhao, S. N.; Wang, G.; Poelman, D.; Van Der Voort, P. Metal Organic Frameworks Based Materials for Heterogeneous Photocatalysis. *Molecules* **2018**, *23* (11), 2947.
- (37) Chen, Y.; Wang, D.; Deng, X.; Li, Z. Metal-Organic Frameworks (MOFs) for Photocatalytic CO₂ Reduction. *Catal. Sci. Technol.* **2017**, *7* (21), 4893–4904.
- (38) Reddy, C. V.; Reddy, K. R.; Harish, V. V. N.; Shim, J.; Shankar, M. V.; Shetti, N. P.; Aminabhavi, T. M. Metal-Organic Frameworks (MOFs)-Based Efficient Heterogeneous Photocatalysts: Synthesis, Properties and Its Applications in Photocatalytic Hydrogen Generation, CO₂ Reduction and Photodegradation of Organic Dyes. *Int. J. Hydrogen Energy* **2020**, *45* (13), 7656–7679.
- (39) Yang, H.; Lai, C.; Wu, M.; Wang, S.; Xia, Y.; Pan, F.; Lv, K.; Wen, L. Novel Amino-Functionalized Ni(II)-Based MOFs for Efficiently Photocatalytic Reduction of CO₂ to CO with Superior Selectivity under Visible-Light Illumination. *Chem. Eng. J.* **2023**, *455*, 140425.
- (40) Song, K.; Liang, S.; Zhong, X.; Wang, M.; Mo, X.; Lei, X.; Lin, Z. Tailoring the Crystal Forms of the Ni-MOF Catalysts for Enhanced Photocatalytic CO₂-to-CO Performance. *Appl. Catal. B Environ.* **2022**, *309*, 121232.
- (41) Peng, H.; Zhang, Q.; Fan, Z.; Luo, Y.; Xu, Q.; Li, J.; Xie, Y. A P-Doped BiOBr Nanosheet for Enhanced Photocatalytic CO₂ Reduction Efficiency. *J. Mol. Struct.* **2024**, *1307*, 138041.
- (42) Draper, F.; Doeven, E. H.; Adcock, J. L.; Francis, P. S.; Connell, T. U. Extending Photocatalyst Activity through Choice of Electron Donor. *J. Org. Chem.* **2023**, *88* (10), 6445–6453.
- (43) Kammer, L. M.; Badir, S. O.; Hu, R. M.; Molander, G. A. Photoactive Electron Donor-Acceptor Complex Platform for Ni-Mediated C(Sp³)-C(Sp²) Bond Formation. *Chem. Sci.* **2021**, *12* (15), 5450–5457.
- (44) Verma, A.; Fu, Y. P. Recent Developments in Piezo-Photocatalytic CO₂ Reduction: Concepts, Mechanism, and Advances. *Dalt. Trans.* **2024**, *53* (11), 4890–4899.
- (45) Yang, H.; Lai, C.; Wu, M.; Wang, S.; Xia, Y.; Pan, F.; Lv, K.; Wen, L. Novel Amino-Functionalized Ni(II)-Based MOFs for Efficiently Photocatalytic Reduction of CO₂ to CO with Superior Selectivity under Visible-Light Illumination. *Chem. Eng. J.* **2023**, *455*, 140425.
- (46) Wang, Z.; Fan, J.; Cheng, B.; Yu, J.; Xu, J. Nickel-Based Cocatalysts for Photocatalysis: Hydrogen Evolution, Overall Water Splitting and CO₂ Reduction. *Mater. Today Phys.* **2020**, *15*, 100279.
- (47) Ramyashree, M. S.; Shanmuga Priya, S.; Freudenberg, N. C.; Sudhakar, K.; Tahir, M. Metal-Organic Framework-Based Photocatalysts for Carbon Dioxide Reduction to Methanol: A Review on Progress and Application. *J. CO₂ Util.* **2021**, *43*, 101374.
- (48) Jin, L.; Lv, S.; Miao, Y.; Liu, D.; Song, F. Recent Development of Porous Porphyrin-Based Nanomaterials for Photocatalysis. *Chem-CatChem* **2021**, *13* (1), 140–152.
- (49) Xue, Y.; Zhao, G.; Yang, R.; Chu, F.; Chen, J.; Wang, L.; Huang, X. 2D Metal-Organic Framework-Based Materials for Electrocatalytic, Photocatalytic and Thermocatalytic Applications. *Nanoscale* **2021**, *13* (7), 3911–3936.
- (50) Chen, L.; Yang, J.; Yang, W.; Xian, J.; Li, G. Nickel Metal-Organic Frameworks for Visible-Light CO₂ Reduction under Mild Reaction Conditions. *Dalt. Trans.* **2022**, *51* (20), 7950–7956.
- (51) Shah, S. S. A.; Nazir, M. A.; Khan, K.; Hussain, I.; Tayyab, M.; Alarfaji, S. S.; Hassan, A. M.; Sohail, M.; Javed, M. S.; Najam, T. Solar Energy Storage to Chemical: Photocatalytic CO₂ Reduction over Pristine Metal-Organic Frameworks with Mechanistic Studies. *J. Energy Storage* **2024**, *75*, 109725.
- (52) Li, D.; Kassymova, M.; Cai, X.; Zang, S.-Q.; Jiang, H.-L. Photocatalytic CO₂ Reduction over Metal-Organic Framework-Based Materials. *Coord. Chem. Rev.* **2020**, *412*, 213262.
- (53) Chen, E. X.; Qiu, M.; Zhang, Y. F.; Zhu, Y. S.; Liu, L. Y.; Sun, Y. Y.; Bu, X.; Zhang, J.; Lin, Q. Acid and Base Resistant Zirconium Polyphenolate-Metalloporphyrin Scaffolds for Efficient CO₂ Photoreduction. *Adv. Mater.* **2018**, *30* (2), 1704388.
- (54) Purvika, A.; Yadav, S.; Jijoe, S. P.; Tenzin, T.; Divya, V.; Shahmoradi, B.; Wantala, K.; Jenkins, D.; McKay, G.; Shivaraju, H. P. Improved Metal-Organic Frameworks (MOFs) and Their Application

in Catalytic CO₂ Reduction: A Review. *Mater. Today Sustain.* **2024**, *26*, 100745.

(55) Mirshokraei, S. A.; Muhyuddin, M.; Orsilli, J.; Berretti, E.; Lavacchi, A.; Lo Vecchio, C.; Baglio, V.; Viscardi, R.; Zaffora, A.; Di Franco, F.; Santamaria, M.; Olivi, L.; Pollastri, S.; Santoro, C. Mono-, Bi- and Tri-Metallic Fe-Based Platinum Group Metal-Free Electrocatalysts Derived from Phthalocyanine for Oxygen Reduction Reaction in Alkaline Media. *Nanoscale* **2024**, *16* (13), 6531–6547.

(56) Chen, I. W. P.; Chen, W. Y.; Liu, T. Y. Pioneering Ultra-Efficient Oxygen Evolution Reaction: A Breakthrough in Tri-Metallic Organic Frameworks Synthesis. *Mater. Today Chem.* **2024**, *35*, 101873.

(57) Lim, J. W.; Choo, D. H.; Cho, J. H.; Kim, J.; Cho, W. S.; Ngome Okello, O. F.; Kim, K.; Lee, S.; Son, J.; Choi, S. Y.; Kim, J. K.; Jang, H. W.; Kim, S. Y.; Lee, J. L. A MOF-Derived Pyrrolic N-Stabilized Ni Single Atom Catalyst for Selective Electrochemical Reduction of CO₂ to CO at High Current Density. *J. Mater. Chem. A* **2024**, *12* (18), 11090–11100.

(58) Li, C.; Yu, H.; Guo, S.; Jia, J.; Chang, Y.; Jia, M.; Wang, J. Enhanced Photocatalytic CO₂ Reduction Using a Trimetallic Organic Framework as the Catalyst under Visible Light. *New J. Chem.* **2024**, *48* (8), 3364–3369.

(59) Niu, S.; Li, C.; Huo, J.; Dong, W.; El Hankari, S.; Liang, Y.; Li, Q. Ultrathin Trimetal-Organic Framework Nanosheet Electrocatalysts for the Highly Efficient Oxygen Evolution Reaction. *ACS Omega* **2021**, *6* (22), 13946–13952.

(60) Li, Y.; Ren, D.; Guo, S.; Wang, M.; Zhai, J.; Zhang, S.; Gong, X.; Zhang, X. Preparation of Nickel-Doped Iron-Based Bimetallic Organic Framework Carbonized Derivatives for Heterogeneous Catalytic Hydrogen Peroxide Degradation of 4-NP. *J. Mol. Struct.* **2024**, *1299*, 137058.

(61) Boukayouht, K.; Nor, N. U. M.; Ait-Khouia, Y.; Queen, W. L.; Saidina Amin, N. A.; El Hankari, S. Enhanced Photocatalytic CO₂ Reduction to Methanol over Eco-Friendly CuCo-ZIF@g-C₃N₄ Synthesized from Recyclable Resources. *Inorg. Chem.* **2025**, *64* (9), 4308–4319.

(62) Wang, A.; Zhou, Y.; Wang, Z.; Chen, M.; Sun, L.; Liu, X. Titanium Incorporated with UiO-66(Zr)-Type Metal-Organic Framework (MOF) for Photocatalytic Application. *RSC Adv.* **2016**, *6* (5), 3671–3679.

(63) Yuan, S.; Peng, J.; Zhang, Y.; Shao-Horn, Y. Stability Trend of Metal-Organic Frameworks with Heterometal-Modified Hexanuclear Zr Building Units. *J. Phys. Chem. C* **2019**, *123* (46), 28266–28274.

(64) Dao, X. Y.; Sun, W. Y. Single- And Mixed-Metal-Organic Framework Photocatalysts for Carbon Dioxide Reduction. *Inorg. Chem. Front.* **2021**, *8* (13), 3178–3204.

(65) Fang, Z.-B.; Liu, T.-T.; Liu, J.; Jin, S.; Wu, X.-P.; Gong, X.-Q.; Wang, K.; Yin, Q.; Liu, T.-F.; Cao, R.; Zhou, H.-C. Boosting Interfacial Charge-Transfer Kinetics for Efficient Overall CO₂ Photoreduction via Rational Design of Coordination Spheres on Metal-Organic Frameworks. *J. Am. Chem. Soc.* **2020**, *142* (28), 12515–12523.

(66) Li, N. X.; Chen, Y. M.; Xu, Q. Q.; Mu, W. H. Photocatalytic Reduction of CO₂ to CO Using Nickel(II)-Bipyridine Complexes with Different Substituent Groups as Catalysts. *J. CO₂ Util.* **2023**, *68*, 102385.

(67) Chang, H.; Zhou, Y.; Zhang, S.; Zheng, X.; Xu, Q. CO₂-Induced 2D Ni-BDC Metal-Organic Frameworks with Enhanced Photocatalytic CO₂ Reduction Activity. *Adv. Mater. Interfaces* **2021**, *8* (13), 2100205.

(68) Yang, W.; Wang, H. J.; Liu, R. R.; Wang, J. W.; Zhang, C.; Li, C.; Zhong, D. C.; Lu, T. B. Tailoring Crystal Facets of Metal-Organic Layers to Enhance Photocatalytic Activity for CO₂ Reduction. *Angew. Chemie - Int. Ed.* **2021**, *60* (1), 409–414.

(69) Chen, L.; Liu, Q.; Yang, J.; Li, Y.; Li, G. Thermal Expansion-Quench of Nickel Metal-Organic Framework into Nanosheets for Efficient Visible Light CO₂ Reduction. *Chin. Chem. Lett.* **2023**, *34* (2), 107335.

(70) Guo, K.; Hussain, I.; Jie, G.; Fu, Y.; Zhang, F.; Zhu, W. Strategies for Improving the Photocatalytic Performance of Metal-Organic Frameworks for CO₂ Reduction: A Review. *J. Environ. Sci.* **2023**, *125*, 290–308.

(71) Abdellah, M.; El-Zohry, A. M.; Antila, L. J.; Windle, C. D.; Reisner, E.; Hammarström, L. Time-Resolved IR Spectroscopy Reveals a Mechanism with TiO₂ as a Reversible Electron Acceptor in a TiO₂-Re Catalyst System for CO₂ Photoreduction. *J. Am. Chem. Soc.* **2017**, *139* (3), 1226–1232.

(72) Nganga, J. K.; Samanamu, C. R.; Tanski, J. M.; Pacheco, C.; Saucedo, C.; Batista, V. S.; Grice, K. A.; Ertem, M. Z.; Angeles-Boza, A. M. Electrochemical Reduction of CO₂ Catalyzed by Re(Pyridine-Oxazoline)(CO)₃Cl Complexes. *Inorg. Chem.* **2017**, *56* (6), 3214–3226.

(73) Huang, N.-Y.; Chen, Z.-Y.; Hu, F.-L.; Shang, C.-Y.; Wang, W.; Huang, J.-R.; Zhou, C.; Li, L.; Xu, Q. Large-Scale Synthesis of Low-Cost 2D Metal-organic Frameworks for Highly Selective Photocatalytic CO₂ Reduction. *Nano Res.* **2023**, *16*, 7756–7760.

(74) Song, K.; Qiu, X.; Han, B.; Liang, S.; Lin, Z. Efficient Upcycling Electroplating Sludge and Waste PET into Ni-MOF Nanocrystals for the Effective Photoreduction of CO₂. *Environ. Sci. Nano* **2021**, *8* (2), 390–398.

(75) Han, B.; Ou, X.; Zhong, Z.; Liang, S.; Yan, X.; Deng, H.; Lin, Z. Photoconversion of Anthropogenic CO₂ into Tunable Syngas over Industrial Wastes Derived Metal-Organic Frameworks. *Appl. Catal. B Environ.* **2021**, *283*, 119594.

(76) Chen, S.; Xu, X.; Gao, H.; Wang, J.; Li, A.; Zhang, X. Fine-Tuning the Metal Oxo Cluster Composition and Phase Structure of Ni/Ti Bimetallic MOFs for Efficient CO₂ Reduction. *J. Phys. Chem. C* **2021**, *125* (17), 9200–9209.

(77) Guo, S. H.; Guo, S. H.; Qi, X. J.; Zhou, H. M.; Zhou, J.; Wang, X. H.; Dong, M.; Zhao, X.; Sun, C. Y.; Wang, X. L.; Su, Z. M.; Su, Z. M. A Bimetallic-MOF Catalyst for Efficient CO₂ Photoreduction from Simulated Flue Gas to Value-Added Formate. *J. Mater. Chem. A* **2020**, *8* (23), 11712–11718.

(78) Zhang, J.; Wang, Y.; Wang, H.; Zhong, D.; Lu, T. Enhancing Photocatalytic Performance of Metal-Organic Frameworks for CO₂ Reduction by a Bimetallic Strategy. *Chin. Chem. Lett.* **2022**, *33* (4), 2065–2068.

(79) Wei, T.; Wang, L.; Mao, K.; Chen, J.; Dai, J.; Zhang, Z.; Liu, L.; Wu, X. Polarization-Induced Efficient Charge Separation in an Electromagnetic Coupling MOF for Enhancing CO₂ Photocatalytic Reduction. *J. Colloid Interface Sci.* **2022**, *622*, 402–409.

(80) Wang, W. J.; Zhang, Y. K.; Wu, A. G.; He, L. N. Cost-Effective 2D Ultrathin Metal-Organic Layers with Bis-Metallic Catalytic Sites for Visible Light-Driven Photocatalytic CO₂ Reduction. *Chem. - A Eur. J.* **2022**, *28* (52), e202202650.

(81) Hu, M.; Liu, J.; Song, S.; Wang, W.; Yao, J.; Gong, Y.; Li, C.; Li, H.; Li, Y.; Yuan, X.; Fang, Z.; Xu, H.; Song, W.; Li, Z. Ultra-Thin Two-Dimensional Trimetallic Metal-Organic Framework for Photocatalytic Reduction of CO₂. *ACS Catal.* **2022**, *12*, 3238.

(82) Gu, L.; Deng, G.; Huang, R.; Shi, X. Optimization of Fe/Ni Organic Frameworks with Core-Shell Structures for Efficient Visible-Light-Driven Reduction of Carbon Dioxide to Carbon Monoxide. *Nanoscale* **2022**, *14* (42), 15821–15831.

(83) Feng, H.; Lv, L.; Huang, Y.; Li, T.; Liu, Y.; Wang, Y. CO Driven Tunable Syngas Synthesis via CO₂ Photoreduction Using a Novel NiCo Bimetallic Metal-Organic Frameworks. *J. Colloid Interface Sci.* **2025**, *684* (P1), 283–290.

(84) Zhang, T.; Sun, X.; Weng, S.; Zhang, S.; Xu, C.; Gao, X.; Zhu, N. Enhancing Photocatalytic Performance of Rose-Shaped Co/Ni Bimetallic Organic Framework for Reducing CO₂ to CO under Visible Light. *J. Mol. Struct.* **2025**, *1321*, 140190.

(85) Zhang, T.; Sun, X.; Weng, S.; Zhang, S.; Xu, C.; Gao, X.; Zhu, N. Enhancing Photocatalytic Performance of Rose-Shaped Co/Ni Bimetallic Organic Framework for Reducing CO₂ to CO under Visible Light. *J. Mol. Struct.* **2025**, *1321*, 140190.

(86) Bhattacharyya, A.; Gutiérrez, M.; Cohen, B.; Valverde-González, A.; Iglesias, M.; Douhal, A. How Does the Metal Doping in Mixed Metal MOFs Influence Their Photodynamics? A Direct Evidence for Improved Photocatalysts. *Mater. Today Energy* **2022**, *29*, 101125.

(87) He, Z. H.; Li, Z. H.; Wang, Z. Y.; Wang, K.; Sun, Y. C.; Wang, S. W.; Wang, W. T.; Yang, Y.; Liu, Z. T. Photothermal CO₂ Hydrogenation

to Hydrocarbons over Trimetallic Co-Cu-Mn Catalysts. *Green Chem.* **2021**, *23* (16), 5775–5785.

(88) Moumen, E.; El Hankari, S. New Insight into the Effect of Layer-by-Layer & in-Situ Growth of MOF on Alginate vs Preformed MOF Mixed Alginate Composites on Dye Adsorption. *Inorg. Chem. Commun.* **2024**, *162*, 112229.

(89) Kidanemariam, A.; Lee, J.; Park, J. Recent Innovation of Metal-Organic Frameworks for Carbon Dioxide Photocatalytic Reduction. *Polymers*. **2019**, *11* (12), 2090.

(90) Crake, A.; Christoforidis, K. C.; Gregg, A.; Moss, B.; Kafizas, A.; Petit, C. The Effect of Materials Architecture in TiO₂/MOF Composites on CO₂ Photoreduction and Charge Transfer. *Small* **2019**, *15* (11), 1805473.

(91) Crake, A.; Christoforidis, K. C.; Kafizas, A.; Zafeirotas, S.; Petit, C. CO₂ Capture and Photocatalytic Reduction Using Bifunctional TiO₂/MOF Nanocomposites under UV-Vis Irradiation. *Appl. Catal. B Environ.* **2017**, *210*, 131–140.

(92) Meng, J.; Chen, Q.; Lu, J.; Liu, H. Z-Scheme Photocatalytic CO₂ Reduction on a Heterostructure of Oxygen-Defective ZnO/Reduced Graphene Oxide/Uio-66-NH₂ under Visible Light. *ACS Appl. Mater. Interfaces* **2019**, *11* (1), 550–562.

(93) Jiang, Z.; Wan, W.; Li, H.; Yuan, S.; Zhao, H.; Wong, P. K. A Hierarchical Z-Scheme α -Fe₂O₃-g-C₃N₄ Hybrid for Enhanced Photocatalytic CO₂ Reduction. *Adv. Mater.* **2018**, *30*, 1706108.

(94) Zhao, H.; Yang, X.; Xu, R.; Li, J.; Gao, S.; Cao, R. CdS/NH₂-Uio-66 Hybrid Membrane Reactors for the Efficient Photocatalytic Conversion of CO₂. *J. Mater. Chem. A* **2018**, *6* (41), 20152–20160.

(95) Dou, Y.; Xu, S.-M.; Zhou, A.; Wang, H.; Zhou, J.; Yan, H.; Li, J.-R. Hierarchically Structured Semiconductor@noble-Metal@MOF for High-Performance Selective Photocatalytic CO₂ Reduction. *Green Chem. Eng.* **2020**, *1* (1), 48–55.

(96) Usman, M.; Zeb, Z.; Ullah, H.; Suliman, M. H.; Humayun, M.; Ullah, L.; Shah, S. N. A.; Ahmed, U.; Saeed, M. A Review of Metal-Organic Frameworks/Graphitic Carbon Nitride Composites for Solar-Driven Green H₂ Production, CO₂ Reduction, and Water Purification. *J. Environ. Chem. Eng.* **2022**, *10* (3), 107548.

(97) Li, R.; Zhang, W.; Zhou, K. Metal-Organic-Framework-Based Catalysts for Photoreduction of CO₂. *Adv. Mater.* **2018**, *30* (35), 1705512.

(98) Wang, S.; Wang, X. Multifunctional Metal-Organic Frameworks for Photocatalysis. *Small* **2015**, *11* (26), 3097–3112.

(99) Sun, D.; Liu, W.; Fu, Y.; Fang, Z.; Sun, F.; Fu, X.; Zhang, Y.; Li, Z. Noble Metals Can Have Different Effects on Photocatalysis over Metal-Organic Frameworks (MOFs): A Case Study on M/NH₂-MIL-125(Ti) (M = Pt and Au). *Chem. - A Eur. J.* **2014**, *20* (16), 4780–4788.

(100) Jiang, H.; Xu, M.; Zhao, X.; Wang, H.; Huo, P. Fabricated Local Surface Plasmon Resonance Cu₂O/Ni-MOF Hierarchical Heterostructure Photocatalysts for Enhanced Photoreduction of CO₂. *SSRN* **2022**.

(101) Liang, S.; Chen, Y.; Han, W.; Jiao, Y.; Li, W.; Tian, G. Hierarchical S-Scheme Titanium Dioxide@cobalt-Nickel Based Metal-Organic Framework Nanotube Photocatalyst for Selective Carbon Dioxide Photoreduction to Methane. *J. Colloid Interface Sci.* **2023**, *630*, 11–22.

(102) Li, J.; Huang, H.; Xue, W.; Sun, K.; Song, X.; Wu, C.; Nie, L.; Li, Y.; Liu, C.; Pan, Y.; Jiang, H. L.; Mei, D.; Zhong, C. Self-Adaptive Dual-Metal-Site Pairs in Metal-Organic Frameworks for Selective CO₂ Photoreduction to CH₄. *Nat. Catal.* **2021**, *4* (8), 719–729.

(103) Sun, S.; He, L.; Yang, M.; Cui, J.; Liang, S. Facet Junction Engineering for Photocatalysis: A Comprehensive Review on Elementary Knowledge, Facet-Synergistic Mechanisms, Functional Modifications, and Future Perspectives. *Adv. Funct. Mater.* **2022**, *32* (1), 2106982.

(104) Wang, T.; Wang, C.; Yang, X.; Ma, R.; Yang, Q.; Shi, W.; Xia, Z.; Ma, H.; Wei, Q.; Chen, S. Electronic-Supply Crystal Facet Guiding Enhancement of Interfacial Charge Transfer in Homologous Covalent Heterojunction NiO/Ni-BDC for Efficient Photocatalytic CO₂ Reduction. *Chem. Eng. J.* **2023**, *475*, 146273.

(105) Xu, M.; Sun, C.; Zhao, X.; Jiang, H.; Wang, H.; Huo, P. Fabricated Hierarchical CdS/Ni-MOF Heterostructure for Promoting Photocatalytic Reduction of CO₂. *Appl. Surf. Sci.* **2022**, *576*, 115792.

(106) Ma, W.; Sun, J.; Yao, S.; Wang, Y.; Chen, G.; Fan, G.; Li, Y. Synergistic Interplay of Dual-Active-Sites on Metallic Ni-MOFs Loaded with Pt for Thermal-Photocatalytic Conversion of Atmospheric CO₂ under Infrared Light Irradiation. *Angew. Chemie - Int. Ed.* **2023**, *62* (48), No. e202313784.

(107) Wei, W.; Wei, Z.; Li, R.; Li, Z.; Shi, R.; Ouyang, S.; Qi, Y.; Philips, D. L.; Yuan, H. Subsurface Oxygen Defects Electronically Interacting with Active Sites on In₂O₃ for Enhanced Photo-thermocatalytic CO₂ Reduction. *Nat. Commun.* **2022**, *13* (1), 3199.

(108) Ra, E. C.; Kim, K. Y.; Kim, E. H.; Lee, H.; An, K.; Lee, J. S. Recycling Carbon Dioxide through Catalytic Hydrogenation: Recent Key Developments and Perspectives. *ACS Catal.* **2020**, *10* (19), 11318–11345.

(109) Xi, Y.; Zhang, X.; Shen, Y.; Dong, W.; Fan, Z.; Wang, K.; Zhong, S.; Bai, S. Aspect Ratio Dependent Photocatalytic Enhancement of CsPbBr₃ in CO₂ Reduction with Two-Dimensional Metal Organic Framework as a Cocatalyst. *Appl. Catal. B Environ.* **2021**, *297*, 120411.

(110) Jiang, Y.; Zhou, R.; Zhang, Z.; Dong, Z.; Xu, J. Boosted Charge Transfer and CO₂ Photoreduction by Construction of S-Scheme Heterojunctions between Cs₂AgBiBr₆ Nanosheets and Two-Dimensional Metal-Organic Frameworks. *J. Mater. Chem. C* **2023**, *11* (7), 2540–2551.

(111) Lin, M.; Cao, R.; Luo, Y.; Zhang, T.; Zhuang, Z.; Yu, Y. Built-In Electric Field Directs Electron Transport at Ultrathin Ni(OH)₂/Metal-Organic Framework Interface for Efficient Photocatalytic CO₂ Reduction. *ACS Appl. Energy Mater.* **2022**, *5* (2), 2161–2168.

(112) Wang, Z.; Wang, Y.; Li, W.; Liu, S.; Zhang, L.; Yang, J.; Feng, C.; Chong, R.; Zhou, Y. Integrating Carbon Quantum Dots with Oxygen Vacancy Modified Nickel-Based Metal Organic Frameworks for Photocatalytic CO₂ Reduction to CH₄ with Approximately 100% Selectivity. *J. Colloid Interface Sci.* **2025**, *678*, 689–702.

(113) Li, X.; Zhu, Q.-L. MOF-Based Materials for Photo-and Electrocatalytic CO₂ Reduction. *EnergyChem.* **2020**, *2* (3), 100033.

(114) Cedeno Morales, E. M.; Kharisov, B. I.; Mendez-Rojas, M. A. CO₂ Photoreduction by MOF-Derived Carbon Nanomaterials: A Review. *Mater. Today Proc.* **2021**, *46*, 2982–2997.

(115) Zhang, W.; Yu, Y.; Huang, R.; Shi, X. Efficient Photocatalytic Reduction of CO₂ to CO Using NiFe₂O₄@N/C/SnO₂ Derived from FeNi Metal-Organic Framework. *ACS Appl. Mater. Interfaces* **2021**, *13* (34), 40571–40581.

(116) Wang, Y. C.; Liu, X. Y.; Wang, X. X.; Cao, M. S. Metal-Organic Frameworks Based Photocatalysts: Architecture Strategies for Efficient Solar Energy Conversion. *J. Chem. Eng.* **2021**, *419*, 129459.

(117) Fan, W. K.; Tahir, M. Recent Advances on Cobalt Metal Organic Frameworks (MOFs) for Photocatalytic CO₂ Reduction to Renewable Energy and Fuels: A Review on Current Progress and Future Directions. *Energy Convers. Manag.* **2022**, *253*, 115180.

(118) Chen, J.; Abazari, R.; Adegoke, K. A.; Maxakato, N. W.; Bello, O. S.; Tahir, M.; Tasleem, S.; Sanati, S.; Kirillov, A. M.; Zhou, Y. Metal-Organic Frameworks and Derived Materials as Photocatalysts for Water Splitting and Carbon Dioxide Reduction. *Coord. Chem. Rev.* **2022**, *469*, 214664.

(119) Khan, I. S.; Mateo, D.; Shterk, G.; Shinkhorova, T.; Poloneeva, D.; Garzón-Tovar, L.; Gascon, J. An Efficient Metal-Organic Framework-Derived Nickel Catalyst for the Light Driven Methanation of CO₂. *Angew. Chemie Int. Ed.* **2021**, *60* (51), 26476–26482.

(120) Jiang, H.; Gong, S.; Xu, S.; Shi, P.; Fan, J.; Cecen, V.; Xu, Q.; Min, Y. Bimetal Composites for Photocatalytic Reduction of CO₂ to CO in the Near-Infrared Region by the SPR Effect. *Dalt. Trans.* **2020**, *49* (16), 5074–5086.

(121) Li, Q.; Gao, Y.; Zhang, M.; Gao, H.; Chen, J.; Jia, H. Efficient Infrared-Light-Driven Photothermal CO₂ Reduction over MOF-Derived Defective Ni/TiO₂. *Appl. Catal. B Environ.* **2022**, *303*, 120905.

(122) Chen, S.; Yu, J.; Zhang, J. Enhanced Photocatalytic CO₂ Reduction Activity of MOF-Derived ZnO/NiO Porous Hollow Spheres. *J. CO₂ Util.* **2018**, *24*, 548–554.

- (123) Zhou, L.; Chen, F. F.; Chen, J.; Feng, Y. N.; Li, L.; Yu, Y. Highly Dispersive Ni@C and Co@C Nanoparticles Derived from Metal-Organic Monolayers for Enhanced Photocatalytic CO₂ Reduction. *Inorg. Chem.* **2021**, 60 (14), 10738–10748.
- (124) Lin, X.; Wang, S.; Tu, W.; Wang, H.; Hou, Y.; Dai, W.; Xu, R. Magnetic Hollow Spheres Assembled from Graphene-Encapsulated Nickel Nanoparticles for Efficient Photocatalytic CO₂ Reduction. *ACS Appl. Energy Mater.* **2019**, 2 (10), 7670–7678.
- (125) Jiang, H.; Gong, S.; Xu, S.; Shi, P.; Fan, J.; Cecen, V.; Xu, Q.; Min, Y. Bimetal Composites for Photocatalytic Reduction of CO₂ to CO in the Near-Infrared Region by the SPR Effect. *Dalt. Trans.* **2020**, 49 (16), 5074–5086.
- (126) Qu, J.; Li, S.; Yang, X.; Zheng, C.; Cai, Y.; Sun, W.; Hu, J.; Li, C. M. Hollow Porous Co-Ni Spinel Nanosheet Arrays with Rich Oxygen Defects on Carbon Cloth toward Highly Efficient and Selective CO₂ Photofixation. *Carbon N. Y.* **2022**, 200, 149–155.
- (127) Zhan, W.; Sun, L.; Han, X. Recent Progress on Engineering Highly Efficient Porous Semiconductor Photocatalysts Derived from Metal-Organic Frameworks. *Nano-Micro Letters* **2019**, 11, 1.
- (128) Ramadhan Ikreedeeh, R.; Arif Hossen, M.; Sherryana, A.; Tahir, M. Recent Advances on Synthesis and Photocatalytic Applications of MOF-Derived Carbon Materials: A Review. *Coord. Chem. Rev.* **2024**, 510, 215834.
- (129) Li, P.; Zhang, S.; Xiao, Z.; Zhang, H.; Ye, F.; Gu, J.; Wang, J.; Li, G.; Wang, D. Ni-TiO₂ Catalysts Derived from Metal-Organic Framework for Efficient Photo-Thermal CO₂ Methanation. *Fuel* **2024**, 357, 129817.
- (130) Fan, W. K.; Tahir, M. Recent Trends in Developments of Active Metals and Heterogenous Materials for Catalytic CO₂ hydrogenation to Renewable Methane: A Review. *J. Environ. Chem. Eng.* **2021**, 9 (4), 105460.
- (131) Li, J.; Lin, Y.; Pan, X.; Miao, D.; Ding, D.; Cui, Y.; Dong, J.; Bao, X. Enhanced CO₂ Methanation Activity of Ni/Anatase Catalyst by Tuning Strong Metal-Support Interactions. *ACS Catal.* **2019**, 9 (7), 6342–6348.
- (132) Meng, A.; Zhang, L.; Cheng, B.; Yu, J. Dual Cocatalysts in TiO₂ Photocatalysis. *Adv. Mater.* **2019**, 31 (30), 1807660.